Analysis and Modelling of Light Sources for Visible Light Communication

Thesis report

by

Ron van Mierop

to obtain the degree of Master of Science at the Delft University of Technology to be defended publicly on March 13, 2023 at 10:30

Thesis committee: Prof. Olindo Isabella

Dr. Patrizio Manganiello

Dr. Marco Antonio Zúñiga Zamalloa

Daily Supervisor: Dr. Mirco Muttillo

Project Duration: June, 2022 - March, 2023

Student number: 1546783

An electronic version of this thesis is available at http://repository.tudelft.nl/.

Faculty of Electrical Engineering, Mathematics and Computer Science · Delft University of Technology

Abstract

The considerable increase in the number of devices needing connectivity, such as mobile phones and Internet of Things (IoT) devices, has led to an exponential rise in data volumes during the last years, that will surely continue over the next decade. Therefore, it will be increasingly challenging to provide sufficient RF resources. A novel alternative to RF communications is Visible Light Communication (VLC). VLC is a communication technology that uses visible light as an information carrier. The use of VLC for indoor applications has been rapidly growing during the last years – Light Fidelity (LiFi) technology is an example of VLC application – with photodiodes being the most widely used receiving devices. However, looking at both indoor and outdoor communication, photovoltaic (PV) cells represent a relevant alternative for detecting the information. One of the advantages of using a PV cell as receiver is the huge sensitive area for detection of the information that simplifies alignment between transmitter and receiver.

Different light sources can be used in VLC. Typically, either LEDs or LASERs are considered, depending on the characteristics of the link (such as distance, type of receiver, indoor/outdoor application). These light sources differ in terms of spectrum, directionality, optical power density and bandwidth. The performance of the whole VLC link strongly depends on the characteristics of the light source, since it affects the ability of the receiver, such as a PV-device, to detect the information when it overlaps with the ambient light, that can reach very high values, especially in outdoor applications where the ambient light is the sunlight. Therefore, the modelling and analysis of the performance of different light sources in a PV-based VLC link will pave the way towards the realisation of a PV-based communication system of the future; and it is the focus of this thesis project.

The project goals were achieved by first reviewing the characteristics of light sources, to understand their advantages and drawbacks in (PV-based) VLC. This was followed by the development of models of the VLC data-link, with a focus on the light source, which took into account various factors such as the type of light source, its location relative to the receiver, and its dynamic behaviour. This was followed by the realisation of a test setup, to characterise different light sources, and the models were then used to simulate the light distribution from the actual light sources. Finally, the framework was used to simulate a LED-based solar simulator and an outdoor VLC data-link.

Contents

Li	st of I	Figures	4
1	Intr	oduction	6
	1.1	Visible Light Communication	6
		1.1.1 Benefits	6
		1.1.2 Challenges	7
		1.1.3 Applications	7
	1.2	VLC with PV Receiver	7
		1.2.1 Benefits	7
		1.2.2 Challenges	8
		1.2.3 Applications	8
	1.3	Thesis Objective	8
	1.4	Thesis Outline	8
	1.7	Thesis Outline	O
2	The	oretical Review	10
	2.1	Visible Light Communication	10
	2.2	Driver	10
		2.2.1 Data-Rate	10
	2.3	VLC with Photovoltaic Receiver	12
	2.4	Electroluminescence	14
		2.4.1 White Phosphor LED	15
		2.4.2 RGB LED	16
		2.4.3 OLED	16
		2.4.4 Micro-LED	17
		2.4.5 LASER	17
	2.5	Light	17
		2.5.1 Human-Centric Lighting	18
		2.5.2 Spectral Power Distribution	20
	2.6	Light Propagation	20
		2.6.1 Directivity	20
		2.6.2 Intensity of Propagated Light	21
		2.6.3 Propagation of Reflected Light	22
		2.0.5 Tropagation of Reflected Light	22
3	Mod	lelling	24
	3.1	Spectral Power Distribution	24
	3.2	Light Distribution	25
		3.2.1 Model Input Parameters	25
		3.2.2 Model Output Parameters	27

		3.2.3	Basic Mode of Operation	27
		3.2.4	Multiple Light Sources	28
		3.2.5	Multipath	29
		3.2.6	Time-Dependence	
4	Exp	eriment	l Validation and Model Calibration	33
	4.1	Experi	nental Method	33
	4.2			33
	4.3			33
	4.4			37
	4.5		·	38
	4.6			41
5	Con	clusion	and Recommendations	44
A	Soft	ware		46
	A.1	Light l	istribution	46
			niformity	

List of Figures

1.1	The visible light spectrum used for VLC [4]	6
1.2	Example of VLC applied in an indoor environment (LiFi [10])	7
2.1	The main components of the VLC data link: a modulator and driver are connected to a light source. The light source emits modulated light to the receiver, and then the signal can be demodulated [16]	11
2.2	Basic VLC PV receiver circuit, with the equivalent photodetector circuit outlined in red, the energy harvesting circuit in blue, and the signal receiver in green [14], [16]	12
2.3	Decreasing peak-to-peak voltage of an OFDM signal, transmitted with a LASER transmitter, with increasing ambient sunlight [13].	13
2.4	Decreasing data-rate with increasing ambient light [13]	13
2.5	Two-diode equivalent circuit of a solar cell expanded with junction and diffusion capaci-	
	tances in red [14]	14
2.6	PN Junction in forward-bias region [29]	15
2.7	The SPD and operation of a PC-LED	16
2.8	Example of the SPD of an RGB LED [35]	17
2.9	CIE chromaticity diagram. Dominant wavelengths of yellow light combined with comple-	
	mentary wavelengths of blue light with a specific power ratio produce white light	18
	Eye sensitivity function. The peak human eye response is to green light at 555 nm [41]	19
		20
	Far-field pattern showing the directivity of a LED [45]	21
2.13	Direct and indirect VLC data links [2]. In the indirect path, the reflector receives the light beam at angle ϕ_1 , and reflects it towards the receiver at angle θ_2	23
3.1	Modelled SPDs of white LEDs, (a) a PC-LED and (b) a RGB-LED	25
3.2	Modelled SPDs of (a) a monochromatic blue LED and (b) a monochromatic red LED	25
3.3	Cross-section illustration of the angles and distance between a modelled light source and	
	receiver, with a single light beam (in blue) from source to receiver	26
3.4	First light distribution modelling scenario	28
3.5	The basic light distribution model with (a) a lens with a narrower field of view, and (b) a larger receiver of $64 \times 64 \text{ cm}^2$.	29
3.6	Model of multiple LEDs. (a) shows the light from four LEDs combined, and (b) shows the light from a single such LED above the top left corner.	29
3.7	Non-direct path of a light beam from the source to a reflector, and from the reflector to the receiver.	30
3.8	Multipath model with receivers of different sizes	30
3.9	Multipaths with different reflectance coefficients.	30

3.10	In this series of models, the optical power of the LED varies from 63 W to 105 W	32
4.1	The grid used for measuring light intensity.	34
4.2	A diagram of the driver circuit used for the experiments (based on the design of Dr. Mirco	
	Muttillo)	34
4.3	AM0 SPD ([49]) and the measured SPD of the full-spectrum LED	35
4.4	Spectra of monochromatic deep red and royal blue LEDs, compared with that of a full-	
	spectrum LED	36
4.5	AM0 solar spectrum compared with measured monochromatic LED spectra	36
4.6	Measured SPD of a royal blue LED (see figure 4.5b) compared with the modelled SPD of a	
	blue LED	37
4.7	Measured light distributions of a full-spectrum LED	37
4.8	Measured light distributions of monochromatic LEDs	38
4.9	Model calibration for full Spectrum LED with a 60° lens	39
	Calibration of the full-spectrum LED without a lens	40
	Royal blue LED model calibration	40
	Deep red LED model calibration	41
	Configurations of LEDs above a surface for improving uniformity	42
4.14	The Solar Simulator provides a uniform ambient light of $1000W/m^2$ on which modelled	
	signals can be superimposed	42
4.15	Light with a step-function of varying optical power from 80.5 W to 98.5 W, superimposed	
	on the solar simulator's uniform ambient light of $1000W/m^2$	43

Chapter 1

Introduction

1.1 Visible Light Communication

Visible light communication (VLC) uses modulated visible light, in the range of approximately 400 nm to 700 nm (see figure 1.1), simultaneously for both illumination and data transfer. It is a branch of optical wireless communication (OWC), which also includes data transfer via infrared (IR) and ultraviolet (UV) light. The concept originated with Masao Nakagawa and his team in 2001, and has since been increasingly researched and developed [1]. Light emitting diodes (LED) are often used in such systems, because they are relatively cheap, widely available, and already extremely common in many applications. In order to transmit data, they can be modulated either by being switched on and off at a high frequency, or by increasing and decreasing their driving current, without significant impact on their operating lifetime [2]. Photodiodes are often used as receivers, due to their relatively simple structures, high responsivity and large bandwidths [3].

1.1.1 Benefits

As the demand for data transfer increases exponentially, radio frequency (RF) bands are becoming a scarce resource, while the wavelength range for visible light is orders of magnitude larger than the available radio frequency bands. This gives it the potential for a high signal-to-noise ratio (SNR) and multichannel data links [2]. Since light does not penetrate through walls, it is also immune to interference from signals in adjacent rooms, and provides protection from eavesdropping and signal jamming [5]. Unlike RF communi-

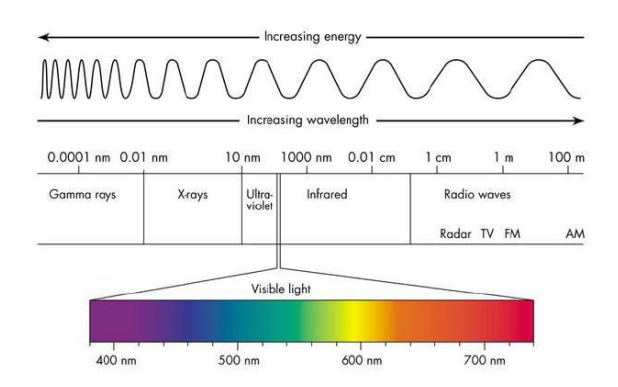


Figure 1.1: The visible light spectrum used for VLC [4].

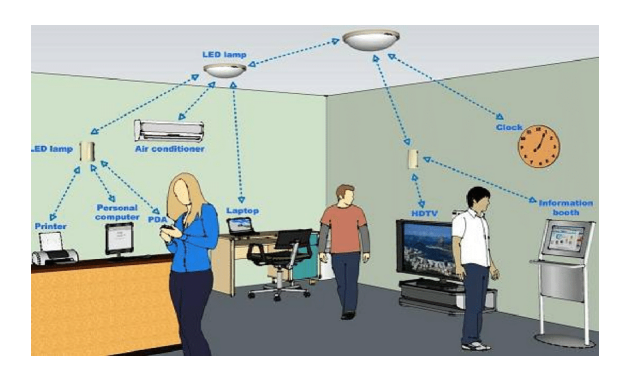


Figure 1.2: Example of VLC applied in an indoor environment (LiFi [10]).

cation, it is license-free, and can work with relatively low-cost, easily available hardware. Lastly, it allows for more efficient use of energy, by reusing the same energy which is already being used for lighting [2].

1.1.2 Challenges

There are several challenges that come with implementing this technology, such as the limited range of light compared to radio waves, due to atmospheric absorption and shadowing [5]; noise due to ambient artificial or natural light; and unidirectionality, as a implementing a return link from a photodiode to a light source is not straightforward [2]. When VLC is used in combination with human-centered lighting, the illumination requirements, such as colour-control and flicker avoidance, need to be taken into consideration in addition to the data-transfer requirements [2].

1.1.3 Applications

This technology has many possible applications, notably where illumination is already present and can easily be utilised for data transfer as well. It can replace Wi-Fi in indoor locations (known as Li-Fi [6], see 1.2). Unlike Wi-Fi, it can be used in places where there is a high sensitivity to electromagnetic interference, such as hospitals and aircraft. It can also be used for low-power sensors or nodes for Internet of Things (IoT) applications [2]. LED-based VLC can provide high-speed data-links in underwater environments, for submarines and related instrumentation [7], while LASER-based VLC can be used for inter-satellite communication, as light scattering is negligible in space [8], [9].

1.2 VLC with PV Receiver

VLC receivers have usually been small photodetectors such as silicon photodiodes or phototransistors, which convert absorbed photons to a small current [2]. LEDs can similarly be used in reverse bias mode as photodetectors [11]. In addition to these, photovoltaic (PV) cells can be used as receivers, with many advantages. This is a part of a quickly growing research field called photovoltatronics [12], which, among other goals, seeks to integrate information technology into photovoltaic energy harvesting.

1.2.1 Benefits

With PV receivers, the energy use of a VLC system can be made much more efficient, as it allows for energy harvesting, either from the light emitted from the transmitter itself, or from sunlight [13]. PV cells are also generally more durable than photodiodes, and have a larger surface area, allowing for easier alignment

and more mobility between the source and the receiver. And unlike photodiodes, PV modules are often specifically designed for outdoor use, which opens up possibilities for VLC in outdoor settings.

1.2.2 Challenges

The response time of PV modules is generally slower than photodiodes [2]. This is due to their capacitance, which acts as a low-pass filter, limiting the frequency response of the module [14]. As the bandwidth of the solar cell depends on the applied bias voltage [15], there is a trade-off between harvesting energy at the maximum power point and communicating with a larger bandwidth. In addition, the integrated electronics required for processing the data can cause the PV cells to heat up, as a result of power dissipation due to parasitic resistance [14], reducing their efficiency.

1.2.3 Applications

PV modules as VLC receivers can be used in a wide variety of applications. Since they are usually designed for outdoor use, they can easily be integrated into vehicles and street lights, allowing for communication among vehicles, and between vehicles street lighting, where VLC in broadcast mode could be relatively simple to implement [2], [12]. Buildings and other urban infrastructure can be covered in such PV modules to enable simultaneous production of electrical energy and data transfer [12]. LASER-based VLC can be used for long-distance communication, for example to provide internet to rural areas by using already existing solar plants.

1.3 Thesis Objective

The optimal design of a VLC system will necessarily depend on the properties of the light sources used and their effect on the performance of the communication link, in terms of energy efficiency, signal bandwidth, bit-rate, light distribution and applicability to different use cases. Therefore, the objective of this thesis is to develop a model that will enable identifying the optimal characteristics and configurations of light sources, so as to improve the performance and range of possible indoor and outdoor use cases for VLC technology, specifically with PV receivers. This should enable the prediction of the behaviour of VLC systems, the identification of the optimal choice of types of light sources and their configurations in such systems, as well as advance the possibility of designing better light sources to be used specifically for VLC purposes.

1.4 Thesis Outline

To accomplish these objectives, this thesis will consist of the following sections:

- 1. Theoretical review: An overview of the theoretical aspects of VLC technology, including the datalink, electroluminescence and light propagation.
- 2. The main part of the thesis consists of models of the spectra of LEDs and the distribution patterns of light propagated from a LED on to a receiver, including a metric of the uniformity of the light over the receiver surface. These models take into account a variety of factors that can affect the light distribution, such as ambient light, the number of light sources and the time-dependent modulated light as used in VLC, which may be especially relevant when combined with PV receivers.
- 3. Experimental validation: In order to validate the models, they are compared to the measured spectra and light distribution patterns of several actual LEDs. Based on these experimental results, the models are refined so as to calibrate their precision in accordance with the measured results, showing how the

models can be used to select specific LED characteristics and configurations for real-world use cases. Lastly, to provide an example of a practical implementation of the preceding models and experiments, a model of a solar simulator is developed, which can be used to facilitate the modelling of outdoor VLC links with a PV receiver.

4. Conclusion and future recommendations: The implications of this analysis are discussed, as well as some of it limitations, and recommendations for future work are given.

Chapter 2

Theoretical Review

2.1 Visible Light Communication

In Visible Light Communication (VLC), a link is formed between the light source and the receiver, by which data is transmitted. The light source is driven by a driver circuit which modulates the light so that information can be encoded in it, while the receiver circuit uses an RC filter to isolate the information in the signal from the received light (see figure 2.1).

2.2 Driver

The light source is generally an LED, which is a current-driven unidirectional conducting device. Its brightness is directly proportional to its forward current, and using a current source for the driving circuit has several advantages over a voltage source, such as a simpler circuit and lower power consumption [17]. An LEDs response time is very short, in the order of *ns*, and the light output can be adjusted by the duty ratio a an input square wave. In some types of signal modulation, such as on-off keying, the light is switched on and off alternately, however this is not ideal when using PV receivers due to their DC characteristics. In order to ensure normal operation, the input voltage should not be lower than the forward voltage drop of the LED. The relationship between the LED current and the luminous flux is not always linear, so the system should be designed so as to operate in the linear region of the LED. To prevent reduced efficiency and damage to the LED, the maximum current and temperatures should be limited [17].

2.2.1 Data-Rate

The performance of a photodetector can be measured by its signal-to-noise ratio, using the following equation [18]:

$$SNR = \frac{\overline{I}_{ph}^2}{\sigma_{shot}^2 \cdot \sigma_{thermal}^2},\tag{2.1}$$

where \bar{I}_{ph} is the average photogenerated current, and σ_{shot}^2 and $\sigma_{thermal}^2$ are the shot noise power and thermal noise power respectively (see eqs. 2.3 and 2.4). The photocurrent I_{ph} is given by the equation [18]:

$$I_{ph}(t) = \frac{\eta q}{hf} P_{R,opt}, \tag{2.2}$$

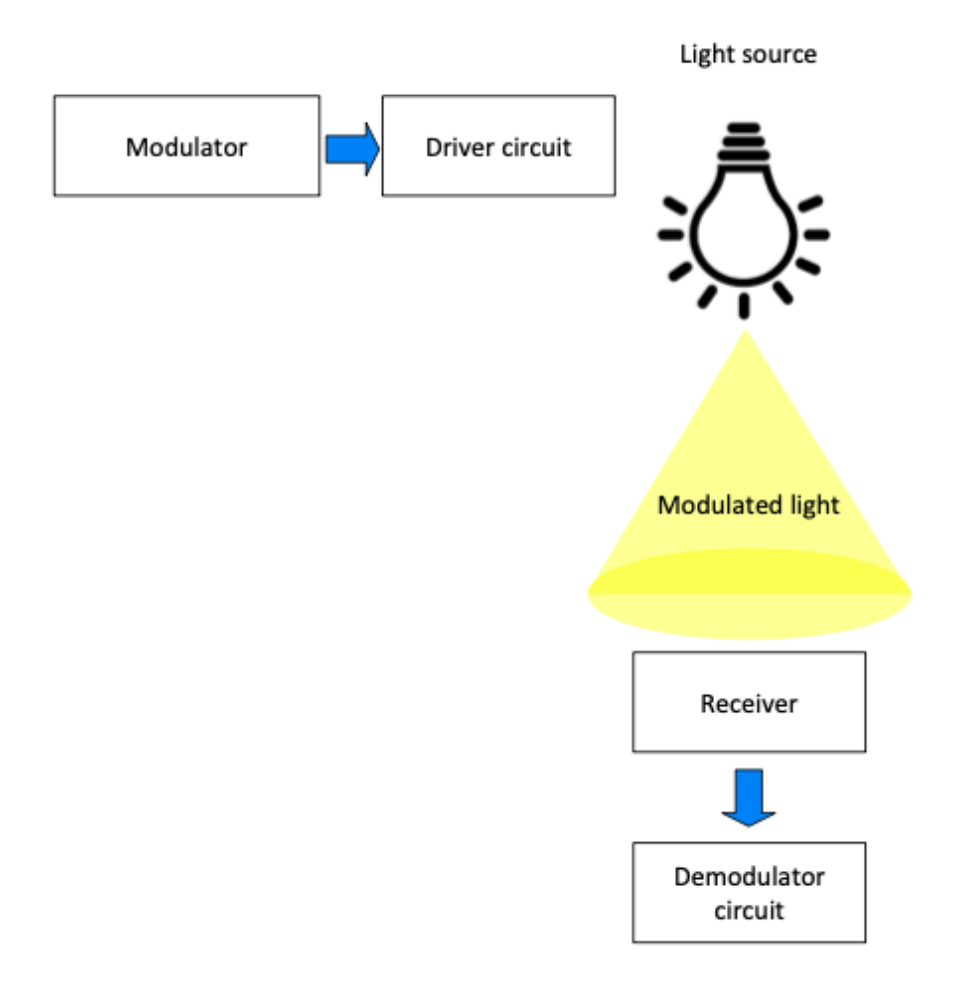


Figure 2.1: The main components of the VLC data link: a modulator and driver are connected to a light source. The light source emits modulated light to the receiver, and then the signal can be demodulated [16].

where η is the quantum efficiency (ratio between the number of electrical carriers generated and the number of photons injected), q is the electron charge $(1.602x10^{-19}C)$, h is the Planck constant (approximately $6.626x10^{-34}JHz^{-1}$), f is the frequency [Hz] and $P_{R,opt}$ is the received optical power [W]. The shot noise power and thermal noise power of a photodetector are given by the equations:

$$\sigma_{shot}^2 = 2q\bar{I}_{ph}B,\tag{2.3}$$

$$\sigma_{thermal}^2 = 4kTBR^{-1}, \tag{2.4}$$

where B is the bandwidth of the electrical filter that follows the photodetector [Hz], k is the Boltzmann constant $(1.38 \cdot 10^{-23} m^2 kg s^{-2} K^{-1})$ or JK^{-1} , T is the absolute temperature [K] and R is the resistance of the photodetector [19], [18]. The shot noise induced by ambient light is the main degrading factor in indoor wireless optical communication systems for bit-rates up to several Mb/s [19].

The maximum data-rate (i.e. channel capacity) is related to the SNR and the bandwidth of the signal, through the equation:

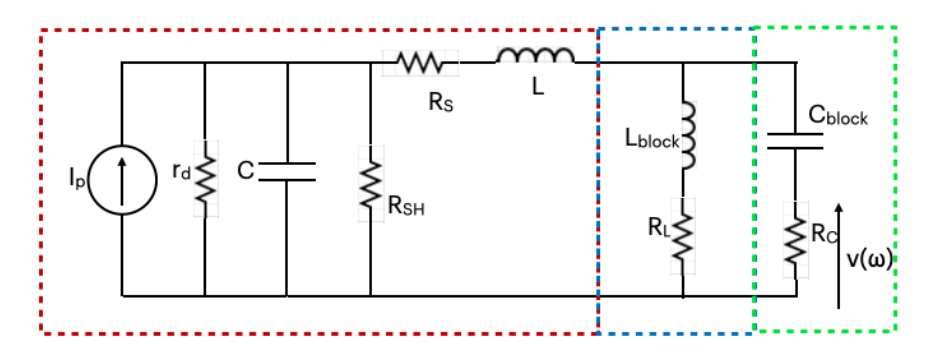
$$C = B\log_2(1 + SNR) \tag{2.5}$$

where C is the channel capacity in bits/sec and B is the bandwidth in Hz [20].

The VLC signal can be encoded with any type of modulation, such as on-off keying, amplitude shift keying (ASK), pulse width modulation (PWM), pulse amplitude modulation (PAM). The bit-error rate (BER), i.e. the number of errors per unit time, of such a data link will depend on the chosen modulation technique.

2.3 VLC with Photovoltaic Receiver

With a photovoltaic (PV) receiver, simultaneously with the data transfer, energy can be harvested from the light using an LC filter in parallel with the RC filter. An example of a photovoltaic receiver is shown in figure 2.2). At low frequencies, an inductor acts as a short circuit, allowing direct current to be used for energy harvesting, while at high frequencies it acts as an open circuit, blocking modulated signals. A capacitor operates inversely, blocking direct current and receiving high frequency currents. In this way, the load R_c and the capacitor C_{block} form the communication branch; while the parallel branch for energy harvesting consists of the inductor L_{block} , which removes ripples from the DC signal, improving the gain of the communication signal, and resistor R_L , which can represent a load or battery. This shows that for the modelling of the communication capabilities of a solar panel, besides the extensively studied and well-established DC characteristics, the AC characteristics of the solar panel must also be taken into account.



Photodetector - Energy Harvesting - Communication Harvesting

Figure 2.2: Basic VLC PV receiver circuit, with the equivalent photodetector circuit outlined in red, the energy harvesting circuit in blue, and the signal receiver in green [14], [16].

The SNR of a VLC system has been shown to decrease (and conversely the BER has been shown to increase) with increasing distance between source and receiver, as the noise due to ambient light remains the same while the signal power decreases [13], [21], [22], [23]. The SNR has also been shown to decrease with higher frequencies when using a PV receiver [24]. The data-rate of a VLC link combined with energy harvesting using a PV receiver has been shown to reach up to 1041 Mb/s, which was achieved with GaAs PV cell [13], [24], however with more specialised PV modules, it could reach higher data-rates. Figure 2.3 shows how outdoor ambient light affects the peak-to-peak voltage of a LASER VLC signal encoded using orthogonal frequency-division multiplexing (OFDM) [24].

The energy harvesting capabilities of the photovoltaic module can conflict with the data transfer capabilities of the system. According to its intensity and spectrum, the signal from the light source will have

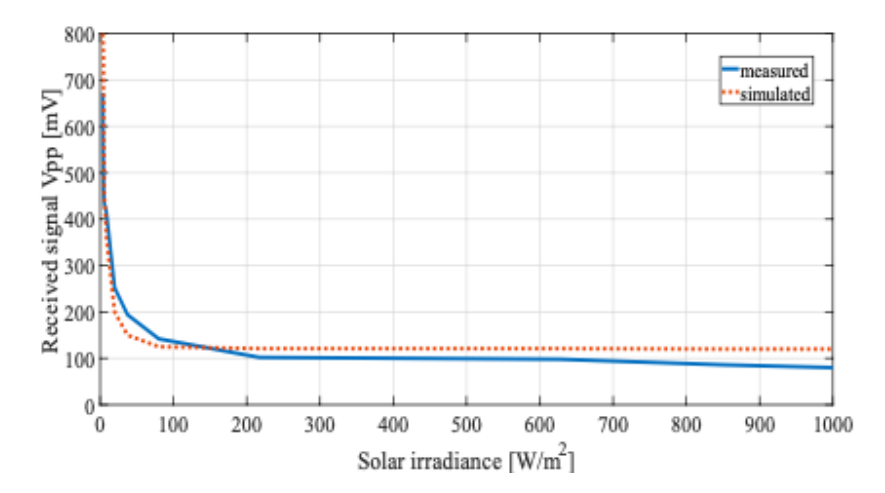


Figure 2.3: Decreasing peak-to-peak voltage of an OFDM signal, transmitted with a LASER transmitter, with increasing ambient sunlight [13].

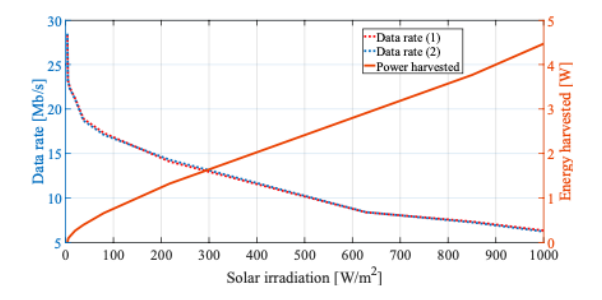


Figure 2.4: Decreasing data-rate with increasing ambient light [13].

to contend with the changing conditions of the ambient light. Figure 2.4, regarding the same signal as in figure 2.3, shows how the data rate decreases as the energy harvesting increases with increasing ambient sunlight [13].

Another factor that can reduce the bit rate of the VLC data link is the capacitance of the PV panel. The capacitance of a pn-junction, such as that in a c-Si solar cell, consists of a junction capacitance and a diffusion capacitance, which makes it act like a low-pass filter, blocking signals above a certain frequency (see figure 2.5). The junction capacitance is given by the equation [14]:

$$C_j = A\sqrt{\frac{q\varepsilon_s N_a N_d}{2(V_{bi} + V_R)}(N_a + N_d)}$$
(2.6)

where A is the cross-sectional area of the pn junction, ε_s is the permittivity of the semi-conductor material, N_a and N_d are the acceptor and donor concentrations respectively, V_{bi} is the built-in voltage of the pn junction and V_R is the applied reverse bias voltage. If the frequency is low enough, i.e. $\omega \tau_{n0} << 1$, $\omega \tau_{p0} << 1$, then the diffusion capacitance can be written as [14]:

$$C_d = \frac{q^2 n_i^2 A}{2kT} \left(\frac{\sqrt{D_p \tau_{p0}}}{N_d} + \frac{\sqrt{D_n \tau_{n0}}}{N_a} \right) exp(\frac{qV_a}{kT}), \tag{2.7}$$

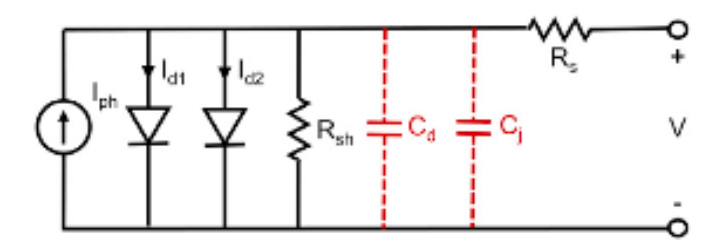


Figure 2.5: Two-diode equivalent circuit of a solar cell expanded with junction and diffusion capacitances in red [14].

where ω is the frequency in radians, n_i is the intrinsic carrier concentration of the semiconductor, T is the temperature [K], D_p and D_n are the hole and electron diffusion constants respectively, τ_{p0} and τ_{n0} are the minority charge carrier lifetimes, and V_a is the applied forward-bias voltage.

The cut-off frequency of such a pv cell depends on its material, and has been previously measured from 1 kHz in an Al-bsf solar cell at 0.54 V of bias voltage to 410 kHz in an amorphous silicon cell with no bias voltage [15].

The overall energy efficiency of a photovoltaic system used for both energy harvesting and data transfer can be found by the equation [12]:

$$EE_{h\nu\to01} = \frac{B\log_2(1 + \frac{P_{sun}A_{PV}\eta_{h\nu\to e}\beta}{BN_o})}{P_{sun}A_{PV}\eta_{h\nu\to e} + c_1B + c_2B\log_2(1 + \frac{P_{sun}A_{PV}\eta_{h\nu\to e}\beta}{BN_o})},$$
(2.8)

where *B* is the communication bandwidth (Hz), P_{sun} is the sunlight intensity on the PV module (W/m^2) , A_{pv} is the area of the PV module that receives power from sunlight (m^2) , β is the communication channel gain (no unit or dB) and N_o is the noise density (WHz^1) . $\eta_{hv\to e}$ is the photovoltatronics efficiency, given by [12]:

$$\eta_{hv\to e} = \eta_{PV} \eta_{WPT} \eta_{WPE} \eta_{IPV}, \tag{2.9}$$

where η_{PV} is the efficiency of the PV system [25], η_{WPT} is the wireless power transfer efficiency [26], η_{WPE} is the LED irreversible thermodynamic wall-plug efficiency [27] and η_{IPV} is the indoor PV efficiency for white LED lighting [25].

2.4 Electroluminescence

The most common light sources for VLC systems are Light Emitting Diodes (LED) and LASER diodes. An LED is a pn junction that emits light when it is subjected to a forward-bias voltage, by a process called electroluminescence, in which electrons and holes are injected across the space-charge region and diffuse into the neutral regions. As the injected minority carriers recombine with majority carriers in a radiative direct band-to-band process, they emit energy as photons [28]. The relation between the diode current and voltage is given by the Shockley equation:

$$I = I_0 exp(\frac{qV_B}{k_b T} - 1), \tag{2.10}$$

Material	Wavelength $\lambda(nm) = hc/Eg$	Material	Wavelength $\lambda(nm) = hc/Eg$
GaAs	838	$GaAs_xP_{1-x}$	650-840
InP	910	GaSb	1600
InAs	3100	InGaAsP	1200-1600
InSb	526	InGaP	500-700
PbSe	8500	ZnSe	490-500
PbTe	6500	$In_xGa_{1-x}N$	450-650

Table 2.1: Several semiconductor materials and the wavelengths at which they produce light [30].

where *I* is the diode current, I_0 is the saturation current density, q is the electron charge $(1.602x10^{-19}C)$, V_B is the bias voltage, T is the temperature [K], and k_b is the Boltzmann constant [16].

The emitted photon energy is related to the band-gap of the semiconductor material by the equation:

$$\lambda = hc/E_g,\tag{2.11}$$

where λ is the wavelength, h is the Planck constant (approximately $6.626x10^{-34}JHz^{-1}$), $c=2.998 \cdot 10^8 m/s$ is the speed of light, and E_g is the band-gap [eV]. Band-gaps between about 1.7 and 3.1 eV correspond to a visible light output of about 400 to 720 nm. Ternary materials can be used to adjust the LED's band-gap, as shown in table 2.1.

LEDs come in every colour, but for human-centred applications they usually emit white light. In general, they are much more efficient, environmentally friendly, cheaper and have longer lifespans than incandescent light bulbs [31]. The most popular types of white LEDs currently in use RGB-LEDs and WP-LEDs. Besides these, there are several newer technologies of LED, discussed below, which may become increasingly popular in the future.

2.4.1 White Phosphor LED

White Phosphor (WP) or Phosphor Coated (PC) LEDs use a blue LED coated with phosphor that emits a yellow light by a process of photoluminescence when it interacts with the blue light of the LED. For this

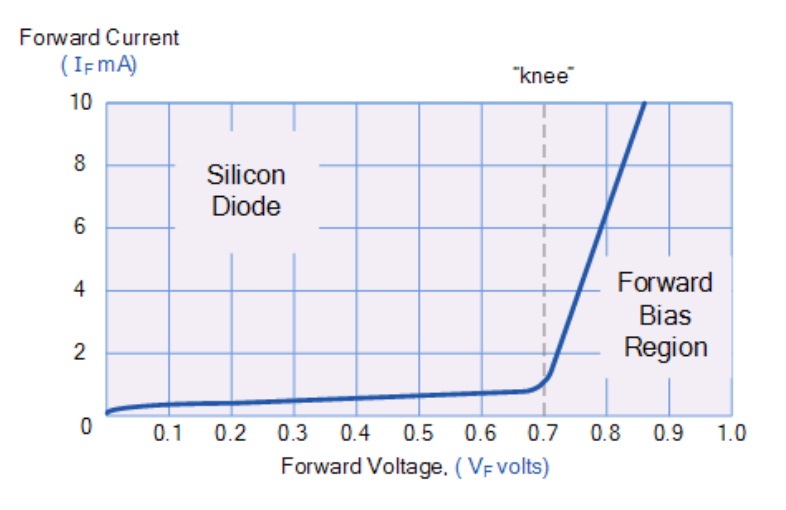
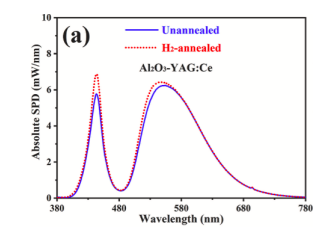
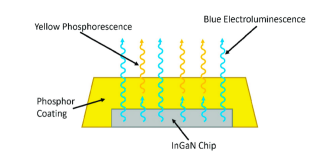


Figure 2.6: PN Junction in forward-bias region [29].





(b) Operation of phosphor-coated LED [33].

(a) Example of the SPD of a YAG:Ce LED[32].

Figure 2.7: The SPD and operation of a PC-LED.

type of LED, a blue LED chip is coated with a yellow fluorescent phosphor, such as $Y_3Al_5O_{12}$: Ce, known as YAG:Ce, is commonly used, due to its broad yellow emission spectrum [17]. The spectrum of the blue LED chip combined with the YAG phosphor gives a typical white light spectrum curve (see figure 2.7a). The yellow spectrum can be adjusted by replacing the cerium with other rare earth elements such as terbium and gadolinium. The disadvantage of this type of LED is the long photoluminescence lifetime of phosphor, in the range of μs , which limits its potential bit rate, i.e. the number of bits transmitted per unit time. This slow photoluminescence process can be overcome by using a dichroic filter (i.e., a filter made of a material which causes light to be split up into distinct wavelength ranges) which isolates the blue light, however this comes at the cost of lower overall efficiency, as the yellow light can then not be used for transferring data [17].

2.4.2 RGB LED

RGB LEDs use an array of three or more monochromatic LEDs combined to create white light. The most common method for obtaining white light is mixing monochromatic red, (amber), green and blue lights. This method requires electronic circuitry to control the colour-mixing ratio, which can increase temperatures and reduce overall efficiency, but it is flexible and can reach high quantum efficiencies [17]. In order for the LED to realistically render the colours of natural daylight, which has a colour rendering index (CRI) of 100, the LED needs to obtain a high CRI, between 80-100. For this purpose, the ratios of red to green to blue should be set to 1:1.2:1 [2]. This method is used in LED displays, as it can produce white light as well as different colors and shades, by adjusting the ratio of the different monochromatic lights. By using more monochromatic lights, a full spectrum can be achieved, simulating sunlight.

RGB LEDs have the advantages of not requiring a slow phosphor conversion process or a dichroic filter as in the white-phosphor LEDs, and each individual LED chip can have a relatively high bandwidth in the mid MHz region, where each wavelength can be used for transmitting data, allowing for higher data rates. There is an issue of cross-talk, where the energy in each wavelength overpass causing superposition of independent data [34].

2.4.3 **OLED**

OLEDs, or organic light-emitting diodes, are a relatively new technology. Efficient electroluminescence from organic semiconductor molecules was first reported by Ching Tang and Steven Van Slyke in 1987, and since then research in this field has been extremely active [36]. OLEDs are extremely thin and flexible, and so they can be integrated easily into many applications. However, due to their material properties and low modulation bandwidth, they cannot reach very data-rates [37].

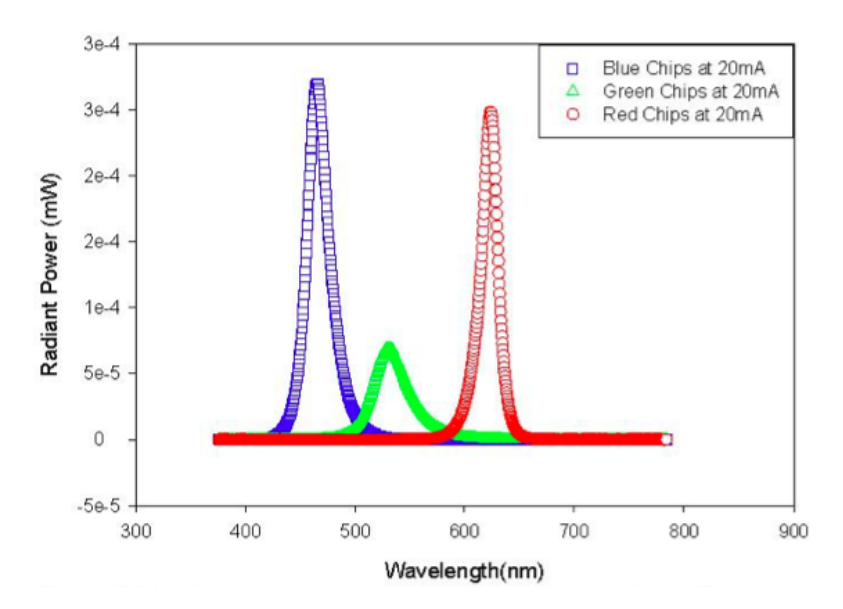


Figure 2.8: Example of the SPD of an RGB LED [35].

2.4.4 Micro-LED

Micro-LEDs, or μ -LEDs, are similar to the RGB-LEDs used for general lighting, only reduced in size to less than 200 μ m. This enables them to reach high efficiencies similar to RGB-LEDs, as well as long shelf-lives. However, their manufacturing processes are currently much more complex and expensive [38]. VLC using μ -LEDs has reached high data-rates, close to those of RGB-LEDs [39].

2.4.5 LASER

Another type of light source which uses electroluminescence is the Light Amplification by Stimulated Emission of Radiation (LASER) diode. In this process, photons are produced similarly to LEDs, in conjunction with an optical cavity consisting of two parallel mirrors, known as a Fabry-Perot resonator [28]. This initiates positive feedback of the light beam, and provides for coherent in-phase light, which can facilitate fast switching frequencies and improve the efficiency of the data-link.

LASERs require complex structures with multilayers of compound semiconductor materials, and their beam is extremely focused, which is not useful for human-centric lighting, and requires precise alignment with the receiver [8]. They are relatively expensive given the same output power as other LEDs, they have high, temperature dependent, input threshold power requirements, and they constitute a dangerous hazard with respect to eye safety. Lastly, LASERs are monochromatic to a high degree, characterised by a single, very narrow, spectral line [2].

2.5 Light

Visible light is the part of the electromagnetic spectrum between about 390 nm (or 770 THz), corresponding to violet light, and 720 nm (or 420 THz), corresponding to red light. Between these are all of the colours of the rainbow, as seen in table 2.3. White light can be produced by a mixture of red, green and blue light, or alternatively by mixing two complementary colours according to the CIE colour graph shown in figure

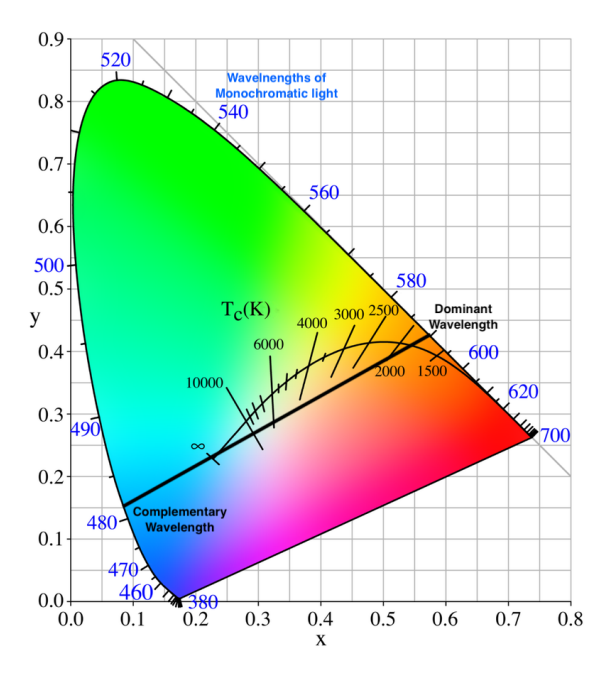


Figure 2.9: CIE chromaticity diagram. Dominant wavelengths of yellow light combined with complementary wavelengths of blue light with a specific power ratio produce white light.

λ_1 (nm)	λ_2 (nm)	P1/P2
400	561.1	0.0785
410	561.3	0.356
420	561.7	0.891
430	562.2	1.42

Table 2.2: Examples of power ratios with which two wavelengths can be mixed in order to produce white light.

2.9. The light resulting from combining light of a dominant wavelength with light of a complementary wavelength depends on the power ratio between the two monochromatic lights, and by adjusting this ratio, white light can be achieved. Some examples of such power ratios are shown in table 2.2.

A monochromatic light source emitting an optical power of 1/683 W at a 555 nm wavelength is said to have a luminous flux θ_v of 1 lumen (lm). 1 lm over 1 m^2 is equal to an illuminance E_v of 1 lux [2].

2.5.1 Human-Centric Lighting

For indoor, human-centric applications, it is important to match the colour and intensity of light to certain recommended guidelines. For normal office spaces, the average light intensity can vary depending on the environment, the age of the people using the light and their specific activities. The recommended illuminance for office work ranges from 300 up to 1500 lux according to the International Organization for Standardisation (ISO) [40]. In addition, the human eye is more sensitive to certain wavelengths than others, as shown in figure 2.10.

Wavelength	Frequency	Colour
Range (nm)	Range (THz)	
200 - 280	1071 - 1500	UV-C
280 - 315	952 - 1071	UV-B
315 - 390	769 - 952	UV-A
390 - 450	666 - 769	Violet
450 - 480	625 - 666	Blue
480 - 500	600 - 625	Cyan
500 - 570	526 - 600	Green
570 - 585	512 - 526	Yellow
585 - 625	480 - 512	Orange
625 - 780	384 - 480	Red
780 - 1720	174 - 384	IR

 Table 2.3: Visible and non-visible colours.

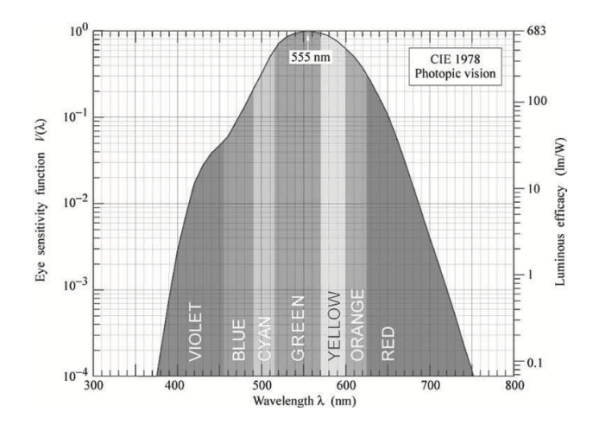


Figure 2.10: Eye sensitivity function. The peak human eye response is to green light at 555 nm [41].

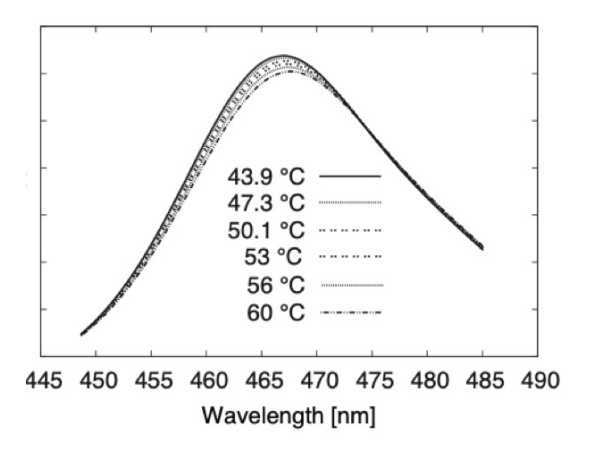


Figure 2.11: Temperature dependence of LED SPD. [43]

2.5.2 Spectral Power Distribution

The spectral power distribution (SPD) is a graphical representation of the emitted power per unit area and unit wavelength radiated by a light source. It can be measured by a spectrometer. Different types of light sources can have very different SPDs. The SPD of an LED has been empirically found to be approximated by a double Gaussian distribution around certain wavelengths, using an equation such as [42]:

$$I(\lambda) = I_{01} exp[-4ln(2)(\frac{\lambda - \lambda_{01}}{\Delta \lambda_{1}})^{2}] + I_{02} exp[-4ln(2)(\frac{\lambda - \lambda_{02}}{\Delta \lambda_{2}})^{2}], \tag{2.12}$$

where $I(\lambda)$ is the intensity at a certain wavelength λ , I_{01} and I_{02} are the peak intensities of the Gaussian distributions at wavelengths of λ_{01} and λ_{02} , and $\Delta\lambda_{01}$ and $\Delta\lambda_{02}$ are full width at half maximum (FWHM) spectral bandwidths. In addition to such a double Gaussian distribution, figure 2.11 shows the dependence of the SPD on temperature. A Gaussian distribution which takes into account the temperature dependence is given by the equation [43]:

$$f(\lambda) = a(I, T_I) \exp[-(\lambda - \lambda_0(I, T_I))^2 / 2c(I, T_I)^2], \tag{2.13}$$

where a is the amplitude of the distribution, c is its width, I is the LED junction current and T_J is given by the equation:

$$T_I = R_{\phi}P + T_{amb},\tag{2.14}$$

where R_{ϕ} is the thermal resistance between the junction and the ambient, P is the electrical power, and T_{amb} is the ambient temperature [43].

2.6 Light Propagation

2.6.1 Directivity

For a Lambertian light source (or reflector), the intensity of light is linearly related to the cosine of the azimuth angle between the light source and the receiver, giving Lambert's cosine law [2]:

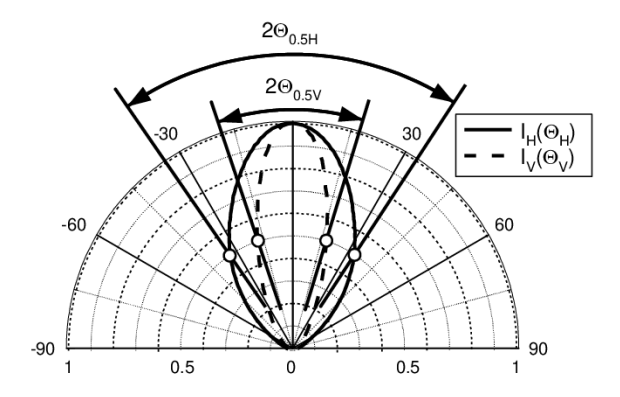


Figure 2.12: Far-field pattern showing the directivity of a LED [45].

$$I_{V}(\theta) = I_{V}(0) \cdot \cos(\theta), \tag{2.15}$$

where $I_{\nu}(\theta)$ is the intensity of light at a given angle θ . A light source (or reflector) obeying the equation:

$$I_{\nu}(\theta) = I_{\nu}(0) \cdot \frac{m+1}{2} \cos^{m}(\theta), \tag{2.16}$$

where m is the mode number, is called a generalised Lambertian [2]. The mode number m is defined by the equation:

$$m = -\frac{1}{\log_2(\cos\theta_{1/2})},\tag{2.17}$$

where $\theta_{1/2}$ is the half-power angle of the light source. The viewing angle of the light source is then given by the equation $2\theta_{1/2}$.

For $\theta_{1/2} = 60^{\circ}$, m = 1, which means that for a Lambertian source, at $\theta = 60^{\circ}$, the intensity is at half of the maximum intensity. When m > 1, $\theta_{1/2} < 60^{\circ}$, and the source is more directional, i.e. the relative intensity decreases faster with a higher angle of incidence [2]. When an LED is used without a lens, it is nearly Lambertian [2]. A wider angle of view results in a more uniform distribution of light [44].

2.6.2 Intensity of Propagated Light

The intensity of light at a certain distance and angle from the light source can be calculated by the equation [2]:

$$P_{R,opt} = P_{T,opt}G_{conc}G_{filter}f(\theta, \theta_{1/2})\frac{A_{R,eff}}{\pi d^2},$$
(2.18)

where the factors that influence the intensity of the light that reaches the receiver are the following:

The function f: a measure of the directivity of the light beam, which depends on the characteristics of the light source, namely, whether it is Lambertian, its half-power angle $\theta_{1/2}$, and the angle of irradiance θ . For a generalised Lambertian light source,

$$f(\theta, \theta_{1/2}) = \frac{1}{2}(m+1)\cos^{m}(\theta). \tag{2.19}$$

 $G_{conc} \ge 1$: a constant concentration factor, due to the lens focusing the light rays. An ideal concentrator with a refractive index n has a gain of [2]:

$$G_{conc} = n^2 / \sin^2(\phi_{FoV}), \tag{2.20}$$

where ϕ_{FoV} is the (one-sided) field of vision angle of the receiver.

 $G_{filter} \leq 1$: a constant optical filtering factor, due to the material of the lens.

d: the distance between the light source and the center of the receiver.

 $P_{T,opt}$: the optical power of the transmitter/light source, which depends on the input voltage and current of the LED.

 $f(\theta, \theta_{1/2})$: a measure of the directivity of the light source, as described in section 2.6.1.

 $A_{R,eff} = A_R \cdot cos\phi$: the effective aperture area of the receiver, where A_R is the photosensitive area of the receiver and ϕ is the angle of incidence.

If the angle of the field of view of the receiver $\phi_{FoV} > 90^{\circ}$, or if θ exceeds the field of view of the receiver, then $P_{R,opt} = 0$.

2.6.3 Propagation of Reflected Light

In indoor applications, another factor that can influence the received optical power is reflections, for example when the light encounters walls or other obstacles. This complicates the calculation of the received power, since the reflector acts as a virtual light source, but with a wavelength-dependent reflectance coefficient ρ , due to absorption in the surface of the reflector. Most reflections are diffuse, and these can typically be modelled as Lambertian, although specular reflections, where the angle of output from the reflector θ_2 is equal to the angle of incidence ϕ_1 , can also occur [2] (see figure 2.13). The received power of light reflected from a point can be calculated by extending equation 2.18 in this way [2]:

$$P_{R,opt} = P_{T,opt}G_{conc}G_{filter}f(\theta_1, \theta_{1/2})\frac{A_{refl,eff}}{\pi d_1^2} \cdot \rho(\lambda)f(\theta_2, \theta_{60^\circ})\frac{A_{R,eff}}{\pi d_2^2},$$
(2.21)

for d_1 , $d_2 \gg \lambda$ and A_R , $A_{refl} \gg \lambda^2$ (which is almost always true for wavelengths in the visible light range), where θ_1 is the angle between the light source and the reflector, θ_2 is the angle between the reflector and the receiver, $A_{refl,eff}$ is the effective area of the reflector, d_1 is the distance between the light source and the reflector, d_2 is the distance between the reflector and the receiver.

For phosphor-based white LEDs in the main spectral range of visible light (approximately 410-780 nm), values of $\rho(\lambda)$ have been empirically found between 0.1 and 0.8 [2]. As $\rho(\lambda)$ is smaller than 1, the intensity of reflected light is normally lower than that of the direct line-of-sight from the source.

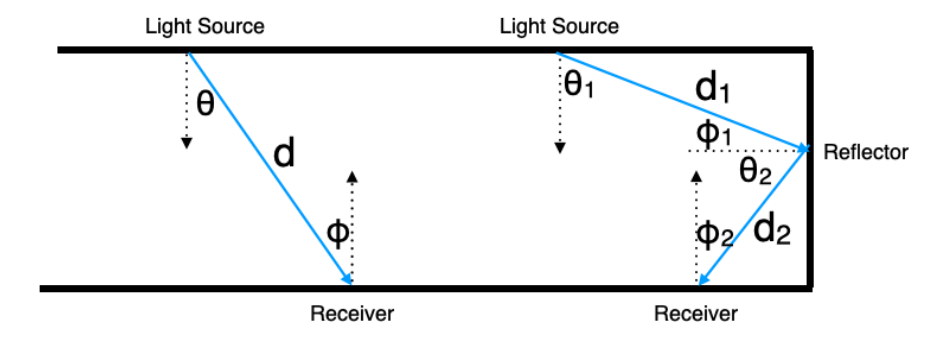


Figure 2.13: Direct and indirect VLC data links [2]. In the indirect path, the reflector receives the light beam at angle ϕ_1 , and reflects it towards the receiver at angle θ_2 .

Chapter 3

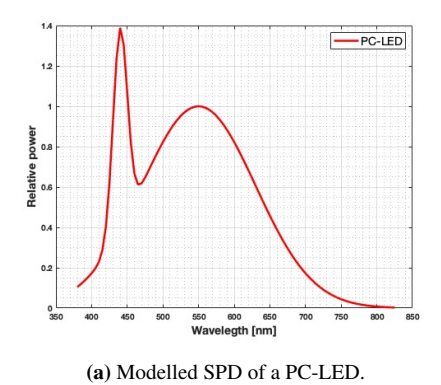
Modelling

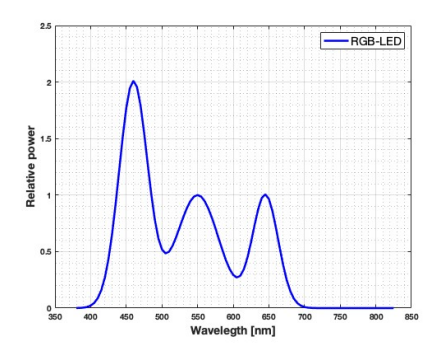
This section presents models developed for the purpose of predicting the behaviour and improving the design of light sources in a VLC system. This includes the characteristics of LEDs to be used as light sources, and their configuration or placement in relation to the VLC receiver. First, the spectral power distributions (SPD) of white (RGB-LEDs and PC-LEDs) and monochromatic (blue and red) LEDs are modelled. Next, the distribution of light from the source to the receiver was modelled, while considering various modes of operation and light source configurations. The models were programmed in MATLAB, and their main functions are presented in appendix A.

3.1 Spectral Power Distribution

For analysing the characteristics of VLC light sources, first a basic model of the SPD of various LEDs is developed. The SPD determines how much power a light source emits per unit area and unit wavelength. For a PC-LED, the SPD is approximated by the combination of two Gaussian distributions, one with a sharp peak in the blue range of the spectrum, and a broader one in the yellow range which is due to the interaction of the blue light with the phosphor coating (see 2.5.2). The SPD of a RGB-LED is approximated by the combination of Gaussian distributions in the range of each of the monochromatic lights which combine to produce white light. The two monochromatic LEDs are similarly modelled with a Gaussian distribution around their respective peaks. As described in equations 2.12 and 2.13, more precise models would include temperature dependence and a double-factor Gaussian distribution [42], [43].

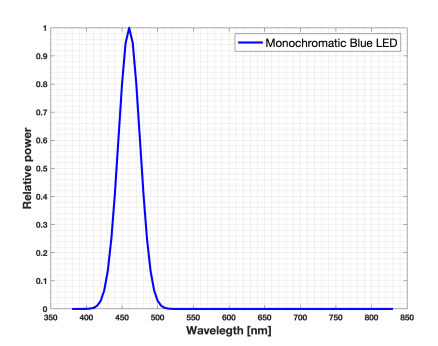
In figure 3.1a, for the SPD of a PC-LED, a narrow Gaussian distribution with a width of 10nm and a peak at 440 nm was modelled to simulate the peak of the blue light in a PC-LED. To this was added a broader Gaussian distribution with a width of 80nm at a peak of 550nm, to simulate the yellow light emitted due to the reaction of the phosphor. In figure 3.1b, the SPD of a RGB-LED was modelled by a combination of three Gaussian distributions, one for each monochromatic light. One distribution with a peak at 440 and a width of 20nm to simulate a blue light, one with a width of 24nm and a peak at 520nm to simulate a green light, and one with a width of 15nm and a peak at 645nm to simulate red light. The values of the Gaussian distributions of the monochromatic lights that make up an RGB-LED can vary, and so these values were chosen knowing that they can be easily adjusted based on future experimental results. Similarly, figures 3.2a and 3.2b used Gaussian distributions with a width of 15nm around 450nm and 645nm respectively, to simulate monochromatic LEDs.

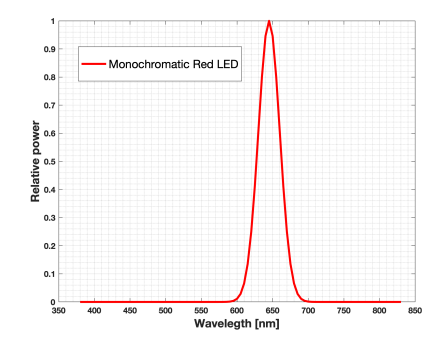




(b) Modelled SPD of a RGB-LED.

Figure 3.1: Modelled SPDs of white LEDs, (a) a PC-LED and (b) a RGB-LED.





- (a) Modelled SPD of a monochromatic blue LED with the peak at 460 nm.
- (b) Modelled SPD of a monochromatic red LED with the peak at 645 nm.

Figure 3.2: Modelled SPDs of (a) a monochromatic blue LED and (b) a monochromatic red LED.

3.2 Light Distribution

The distribution of light propagated from the source onto a receiver is modelled. This is done using the equation that expresses the intensity of light at a certain distance and angle from the light source (see equation 2.18 and figure 3.3). Based on this equation, a grid is constructed corresponding to the surface area of the receiver, and the intensity of light at each grid-point is calculated. Figure 3.3 presents a 2D illustration of the field-of-view θ of the light source, the distance d between the source and the center of the receiver, and the angle of incidence ϕ at a point where the light beam (shown in blue) hits the receiver and the received power is calculated.

3.2.1 Model Input Parameters

The variables used for the different light distribution scenarios are as follows:

• Input power: As noted above, the SPD represents the power of the light source per unit area per unit wavelength. From the integral of the SPD over the entire visible light wavelength range, the overall optical power can be calculated. Similarly, the power in certain intervals of wavelengths can be calculated. This power depends on the input voltage and current, as well as the temperature and characteristics of the LED.

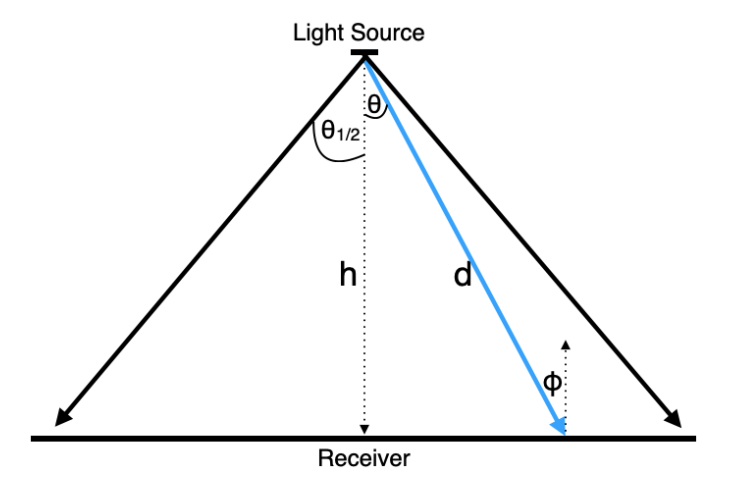


Figure 3.3: Cross-section illustration of the angles and distance between a modelled light source and receiver, with a single light beam (in blue) from source to receiver.

- Position and angle of the source relative to the receiver. This includes the height *d* of the light source, starting from a minimum that will exclude cases where the light cone only reaches a small part of the receiver surface; the location of the light source relative to the center of the receiver, denoted as the x-location and y-location on the plane parallel to the receiver at height d; and the relative angle between the light source and the center of the receiver, correlated with the x axis and y axis of the receiver plane respectively. The field-of-view is denoted by θ. The intensity of light is highest at the center of the field-of-view, and 0 outside of the field-of-view.
- Directivity: Following equations 2.19 and 2.17 in section 2.6.1, f is a function of the angle of irradience and the factor m, and so it is modelled as the exponent with which the intensity of light is decreased as the angle of incidence goes from the center, at which the intensity is highest, to the edge of the viewing angle.
- Lens: A lens can be modelled to focus the light and increase its intensity within a cone. This affects the optical concentration and filtering, as well as the uniformity of light distribution, as described in section 2.6.1.
- Number of sources: All of the aforementioned variables are combined into a class of light sources, and then several light sources with different characteristics and placements can be combined into one model, with their respective intensities superimposed onto the receiver.
- Ambient light: Besides the light from the LED, a uniform ambient light can act like noise when transmitting data.
- Reflectance: In the presence of walls or obstacles, the light can be reflected before reaching the receiver. The intensity of the reflected light depends on the wavelength of light and a reflectance coefficient $\rho(\lambda)$ of the reflecting material, as described in section 2.6.3. This was modelled as an additional Lambertian light source at a point a certain distance and angle from the original light source, simulating the reflected light. This virtual light source has the intensity of the light that reaches it from the original source multiplied by the reflectance coefficient ρ .

3.2.2 Model Output Parameters

The output parameters that the models are used to calculate are the following:

• Overall efficiency of the received light relative to the optical power of the LED, given by the formula:

$$\eta = P_{R.opt}/P_{T.opt},\tag{3.1}$$

where $P_{R,opt}$ is the received optical power, and $P_{T,opt}$ is the transmitted optical power.

- Received intensity at each point of the grid. For the purposes of visualisation, the receiver surface area is represented by a 32 cm by 32 cm grid (except when otherwise specified), divided into 17 by 17 points, and the intensity of light is calculated at each of the 289 grid coordinates. The higher the intensity, the better the data transmission can be, as it will be more resistant to noise from ambient light, as discussed in section 2.3. An example of such a grid is shown in fig 3.4.
- Uniformity of the light distribution over the surface of the receiver. To determine the optimal uniformity, a metric U was formulated, by employing the equation:

$$U = \frac{1 - \Sigma(|I_{x,y} - I_{A\nu}|/I_{A\nu})}{(N_x \cdot N_y)} \cdot 100, \tag{3.2}$$

where $I_{x,y}$ represents the intensity at each point, I_{Av} is the average intensity, and N_w and N_l are the number of points on the grid in the x and y axes respectively. Higher uniformity will allow for easier alignment between source and receiver, and will indicate a larger signal range and an improved potential for the mobility of the receiver within the range of the signal. The maximum uniformity, when the intensity at each point is the precisely the same, is 100, however the minimum is not 0, rather it can become negative when there is a very large variation of intensity over the receiver.

This metric of uniformity differs from previously suggested uniformity metrics (as in [46]), where the uniformity is measured as:

$$U = \frac{I_{min}}{I_{Av}},\tag{3.3}$$

where I_{min} is the minimum intensity and I_{Av} is the average intensity. By considering the relation between the intensity at each point and the average intensity, the uniformity metric can provide more information about the actual distribution of light over the receiver. According to the metric given in [46], the uniformity should be above 70% for office work [40].

3.2.3 Basic Mode of Operation

Before developing more sophisticated models, the first light distribution scenario incorporates only the basic elements of a VLC system: a single LED, directly above the receiver, at a height of 0.25*m*, with a direct line-of-sight and an angle-of-incidence of precisely 90°. A lens with a view-angle of 120° (m=1) and filter and concentration coefficients equal to 1 were also taken into consideration. All other variables, such as ambient light, obstacles and reflectors, were disregarded.

As seen in figure 3.4, the overall efficiency, i.e. the received power divided by the input power of the LED, is approximately 33.16%. In this scenario, the optical power of the LED is 100W, and so the overall received power is approximately 33.16W The power at the center of the grid is over 5 times higher than at the corners, and this corresponds to a uniformity of approximately 66.51.

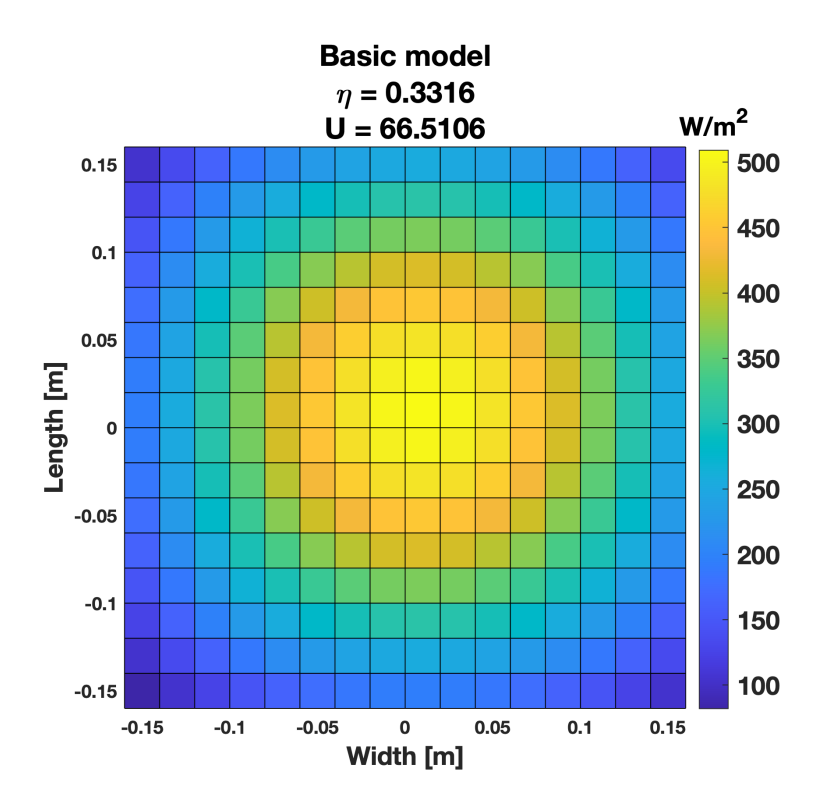


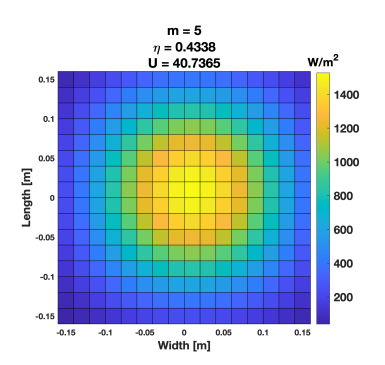
Figure 3.4: First light distribution modelling scenario.

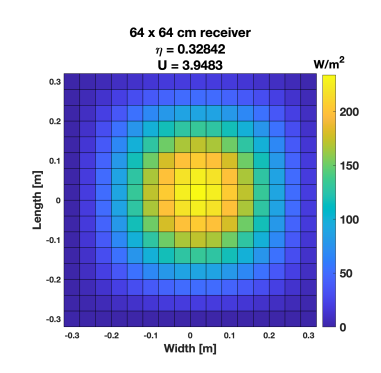
Figure 3.5a shows the a model with the same parameters, except the mode number m is increased to 5, which means the light is more focused, with a lens with a half-power angle of approximately $\theta_{1/2} = 30^{\circ}$ (see equation 2.17). With a more directed light beam, the maximum power at the center of the receiver is greatly increased, while the power decreases with a higher exponent as the angle of incidence is increased. As seen in figure 3.5a, this leads to both a higher efficiency but a lower uniformity in comparison to the scenario with a wider half-power angle.

Next, the area of the receiver surface was extended by doubling its length and width to 0.64 m. For this scenario, the height of the light source was increased, because in keeping the same distance between the source and the receiver, much of the surface area falls outside of the field-of-view of the light source, and so no light reaches it. The larger surface area allows for less light to fall outside of the sensitive receiver area, and so the efficiency is shown to be higher than in the previous scenarios despite the larger distance between source and receiver. However, with the corners of the receiver receiving little or no light, the uniformity is much lower.

3.2.4 Multiple Light Sources

The next model includes multiple light-sources at various distances from the receiver. The intensities of the light from all the sources are superimposed onto the modelled receiver. Figure 3.6a shows a model of the light from four LEDs, each placed above a corner of the receiver, superimposed onto the receiver surface. This presents a much lower efficiency compared with the single-LED scenario, as much of the light from each LED does not reach the receiver, however the uniformity, at over 93, is much higher, i.e. the intensity of the light is spread out more evenly over the receiver surface, despite this scenario taking into account

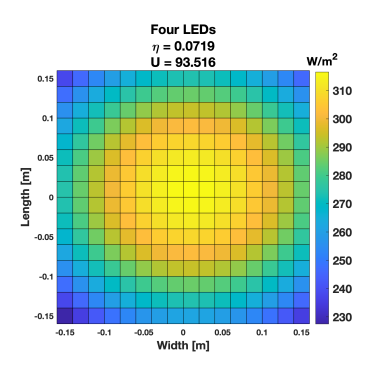


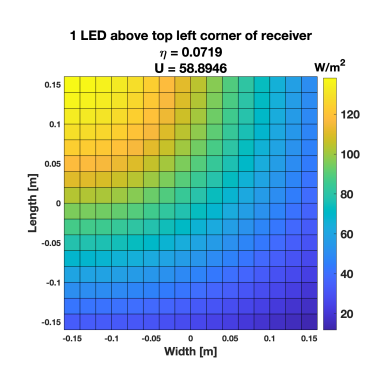


(a) Light distribution with half-power angle $\theta_{1/2}=30^{\circ}.$

(b) Light distribution over a larger, $64 \times 64 \text{ } cm^2$ surface, from a height of 35 cm.

Figure 3.5: The basic light distribution model with (a) a lens with a narrower field of view, and (b) a larger receiver of $64 \times 64 \text{ cm}^2$.





(a) In this model, the light from four LEDs placed above the (b) This model shows the light distribution single LED corners of the receiver are superimposed on the receiver.

Figure 3.6: Model of multiple LEDs. (a) shows the light from four LEDs combined, and (b) shows the light from a single such LED above the top left corner.

smaller distance of 0.21 m between the light sources and the receiver, so 0.04 m lower than in the basic scenario with one LED. Figure 3.6b shows the light from one of the four LEDs of the four-LED model of figure 3.6a.

3.2.5 Multipath

In this case, instead of a direct line-of-sight, single-reflection multipaths were taken into account, (see section 2.6.3). For modelling multipaths, the light source is assumed to be monochromatic, and so $\rho(\lambda)$ is taken to be constant. The reflections are considered Lambertian. In Lambertian reflectance, light is reflected as though from a Lambertian light source. In diffuse reflectance, light can be reflected in many angles. Figure 3.7 shows the path of a light beam reflected from a single point above the edge of a receiver, as would be the case if a small flat obstacle were placed there. If the reflective surface were larger, or had a complex shape, it could lead to more complex patterns.

Figure 3.8a shows the combined light distribution of the direct line-of-sight light path and the light from a single reflection from a point reflector on the left side of the receiver. Figure 3.8b shows the same

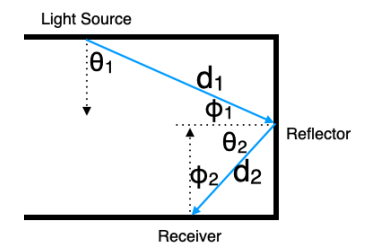
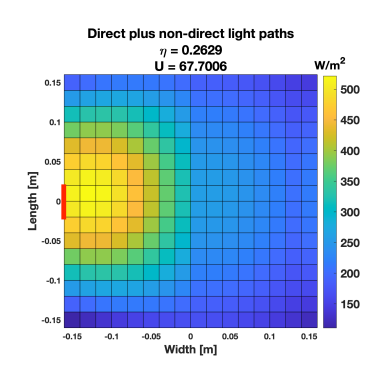
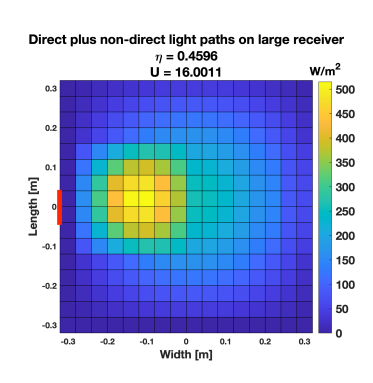


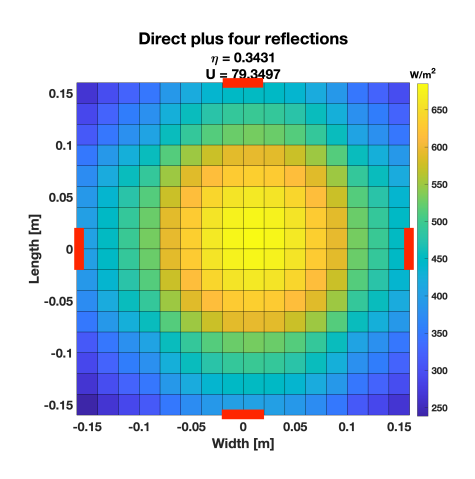
Figure 3.7: Non-direct path of a light beam from the source to a reflector, and from the reflector to the receiver.

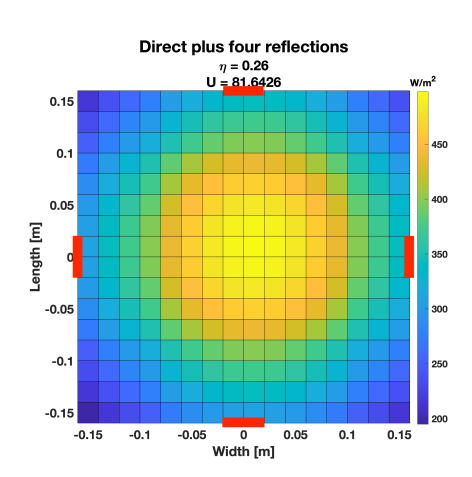




- (a) In this model, light is emitted from the source to the receiver through a direct path, and by way of a single-reflection from the source to a 64 x 64 cm² receiver.

Figure 3.8: Multipath model with receivers of different sizes.





(a) The light distribution from a single light source with an (b) The light distribution from a single light source with an optical power of 100 W, plus its reflection off of four points optical power of 100 W, plus its reflection off of four points above the center of each side of the receiver with reflectance above the center of each side of the receiver with reflectance coefficient $\rho = 1$. coefficient $\rho = 0.5$.

Figure 3.9: Multipaths with different reflectance coefficients.

combination of light beams on a larger receiever. Figure 3.9a shows the light from the direct line-of-sight light distribution combined with four such point-reflections, at a height of 0.16m above each of the sides of the receiver.

In the multipath models in figures 3.8a and 3.8b, the reflecting points had a reflectance coefficient ρ of 0.7 and were placed at 0.16m from the light source. The light source is placed at a height of 0.35m from the receiver, and the reflectance occurs at a height of 0.18m. In the cases of figures 3.9a and 3.9b, the reflectance coefficient was 1 and 0.5 respectively, and the point reflectors were placed at a height of 0.16m above the receiver. As can be seen in these figures, reflections can increase the efficiency of the system, as more of the light from the source is received at the receiver surface.

3.2.6 Time-Dependence

Because a PV receiver can have a filtering effect on the received signal due to its capacitance, the time-dependent characteristics of the output signal should also be considered. Likewise, ambient light can reduce the power of the signal, thereby decreasing the SNR and increasing the BER of the data link (see section 2.3). Therefore, in this scenario, a varying time-dependent intensity of the light-source is modelled. Various types of time-varying signals can be modelled, such as a sinusoidal signal, a triangular function, etc. Likewise, there are various ways in which a time-varying signal can be implemented, such as varying the input current or voltage to the light source, varying the distance between source and receiver, varying a duty ratio input to the light source, etc. The model represented in figure 3.10 employs a simple step-function, whereby the optical power of the light source is increased in equal increments from 63W to 108W.

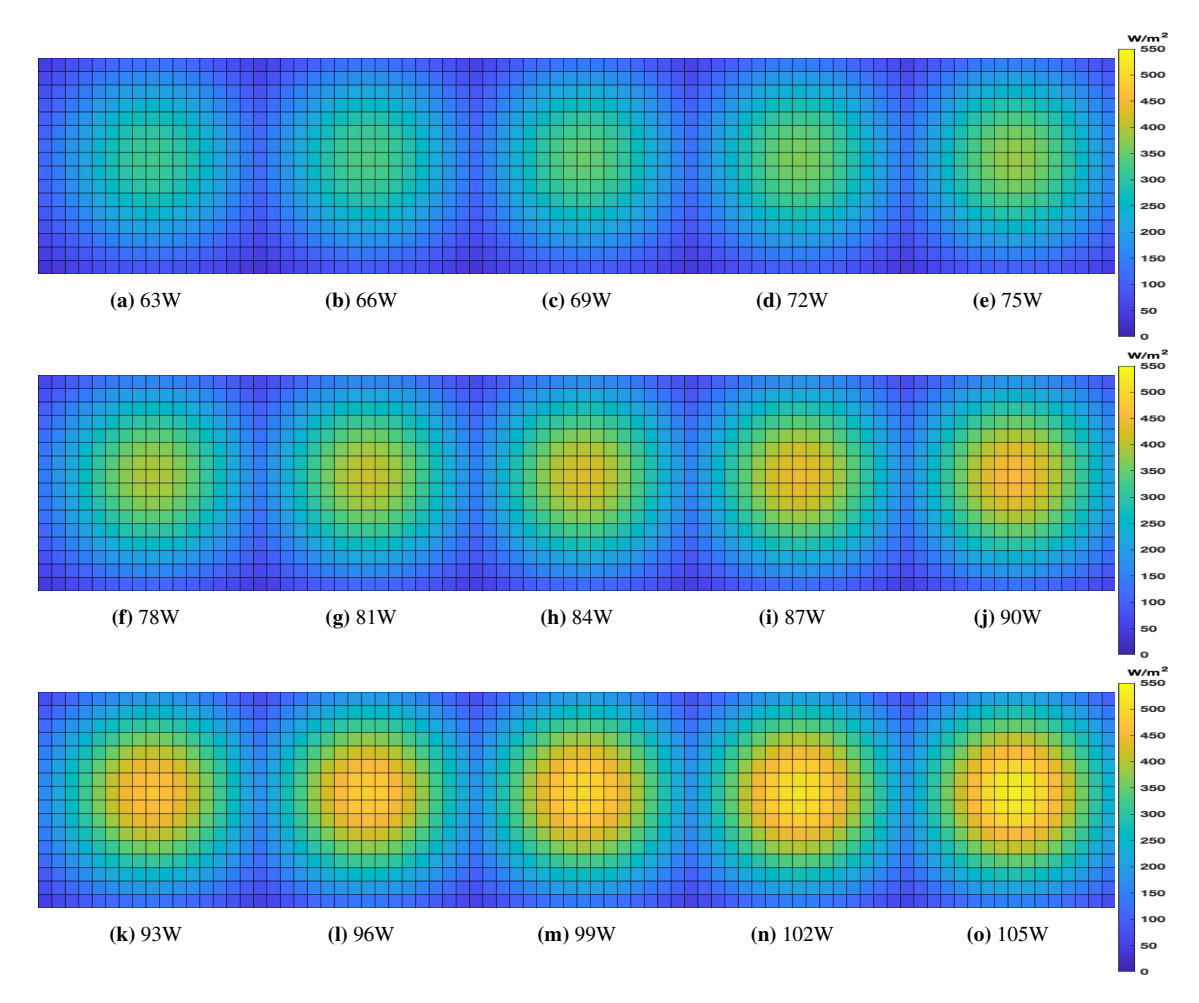


Figure 3.10: In this series of models, the optical power of the LED varies from 63 W to 105 W.

Chapter 4

Experimental Validation and Model Calibration

4.1 Experimental Method

For experimental validation of the models, the spectra and light distribution patterns of several different LEDs were measured in various configurations, corresponding to some of the models described in chapter 3. The results of these measurements were visualised by similar SPD graphs and light distribution grids, and their efficiencies and uniformities were calculated using the same formulas described in chapter 3.2.2. The Root-Mean-Square Error was used to compare the expected results from the models to the experimental results, as described below in section 4.5.

4.2 Setup

The experimental setup consisted of a fixed stand on which various LEDs from LCFOCUS [47] were placed, directly above a 32 cm x 32 cm grid. On various points on this grid a Spectral Evolution SR-1901PT spectrometer [48] was used to measure the received optical power and spectral distribution of the light from the LEDs. The LEDs used were a 100W full-spectrum white LED (model: LC-10FS504-G45), meant to simulate the solar spectrum; a 100W royal blue 440nm monochromatic LED (model: LC-100RB-C45); and a 100W deep red 660nm monochromatic LED (model: LC-100DR-C42). The measurements which involved a lens used a 60° lens. A basic diagram of the current-source driver circuit used for the LEDs is shown in figure 4.2. Such a driver can be small and low-cost, consume little power and have a short response-time [17].

The ambient light within the room in which the experiments were conducted was measured at various times, and was found to range between 0.5W and 1.5W when the room lighting was turned off. This is negligible when compared to the maximum intensities of the LEDs, however it could affect the measurements of low intensities, such as at the corners of the receiver grid.

4.3 SPD

The spectrometer was first used to measure the SPDs of several light sources. The first measurement was of a full-spectrum LED. As opposed to the modelled RGB-LEDs, which combine three monochromatic LEDs, this type of LED uses electronic circuitry and a combination of eight different monochromatic lights, in

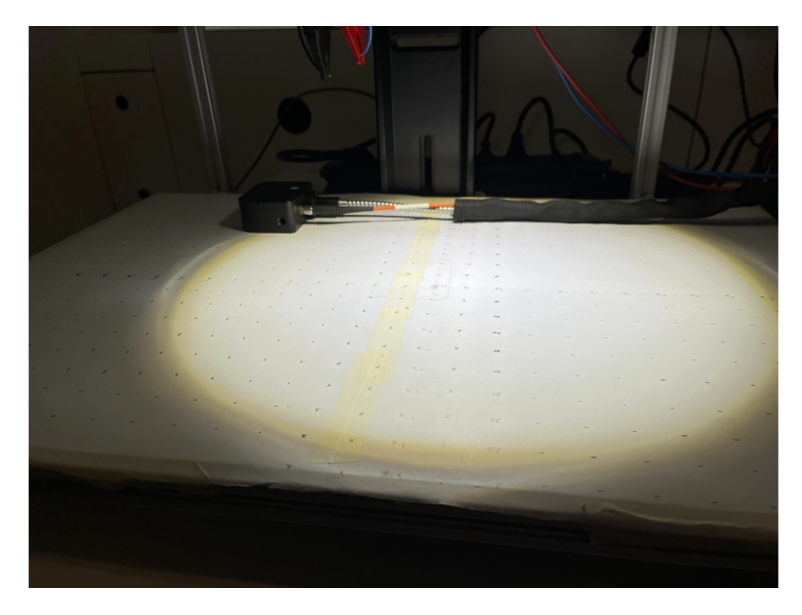


Figure 4.1: The grid used for measuring light intensity.

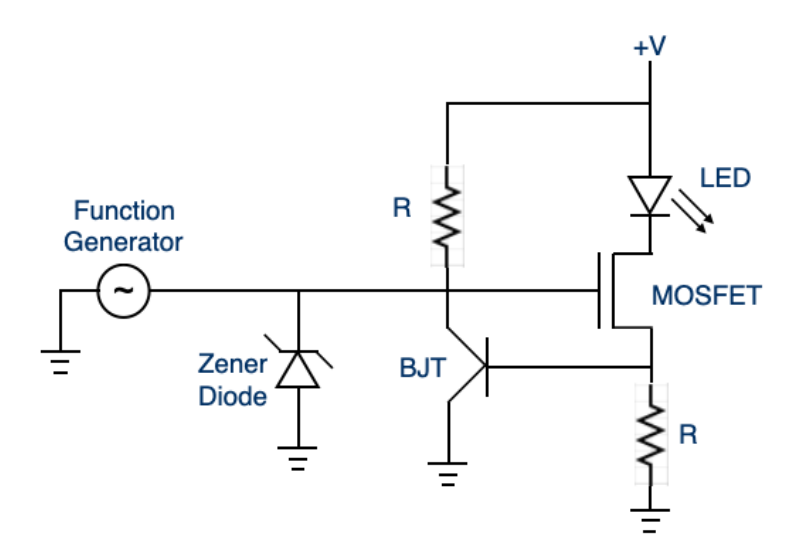


Figure 4.2: A diagram of the driver circuit used for the experiments (based on the design of Dr. Mirco Muttillo).

order to mimic the SPD of sunlight. The measured SPD of this light compared to the AM0 solar spectrum (derived from SMARTS 2.9.2 [49]) is shown in figure 4.3. The SPD of the full-spectrum LED is much more uniform in the visible light range than the white RGB-LED and PC-LED as modelled in section 3.1.

Next, SPDs of several monochromatic LEDs were measured. These show an SPD similar to a Gaussian distribution, as assumed by the models. The shape of the spectra was not affected by the distance or angle between the light source and the spectrometer, however light reflected off of obstacles may have an effect, due to the wavelength-dependent reflectance coefficient.

Figure 4.5a shows the SPD of a Deep Red LED directly above the spectrometer, compared with the SPD of the full-spectrum LED. Despite the lower input power, the peak can be seen to exceed that of the

full-spectrum LED in the range of approximately 650 nm. This shows how monochromatic light has the potential to enable signal transfer despite the presence of ambient sunlight.

In figure 4.5b, the SPD of a Royal Blue LED was measured with the spectrometer at the corner of the 32 by 32 cm grid, i.e. at a distance of approximately 47 cm. In this case, due to the larger distance between the source and the receiver, the peak in the blue wavelength range does not quite exceed that of the full-spectrum LED. This shows that despite the focus of the light over a narrow wavelength band, a high power is still required to overcome the noise generated by ambient light.

Figure 4.6 shows how the model for the monochromatic blue light was adapted according to the measured SPD. The width of the Gaussian curve was reduced to 5nm and the peak was shifted to 427nm. These measurements show how, using a filter, monochromatic light used for signal transfer can overcome ambient light, by isolating the frequencies of the monochromatic light.

The SPDs showed no change when the spectrometer was placed further away from the center, or when the distance between the spectrometer and the light source was increased. Indoor ambient light likewise had very little effect on the total SPD.

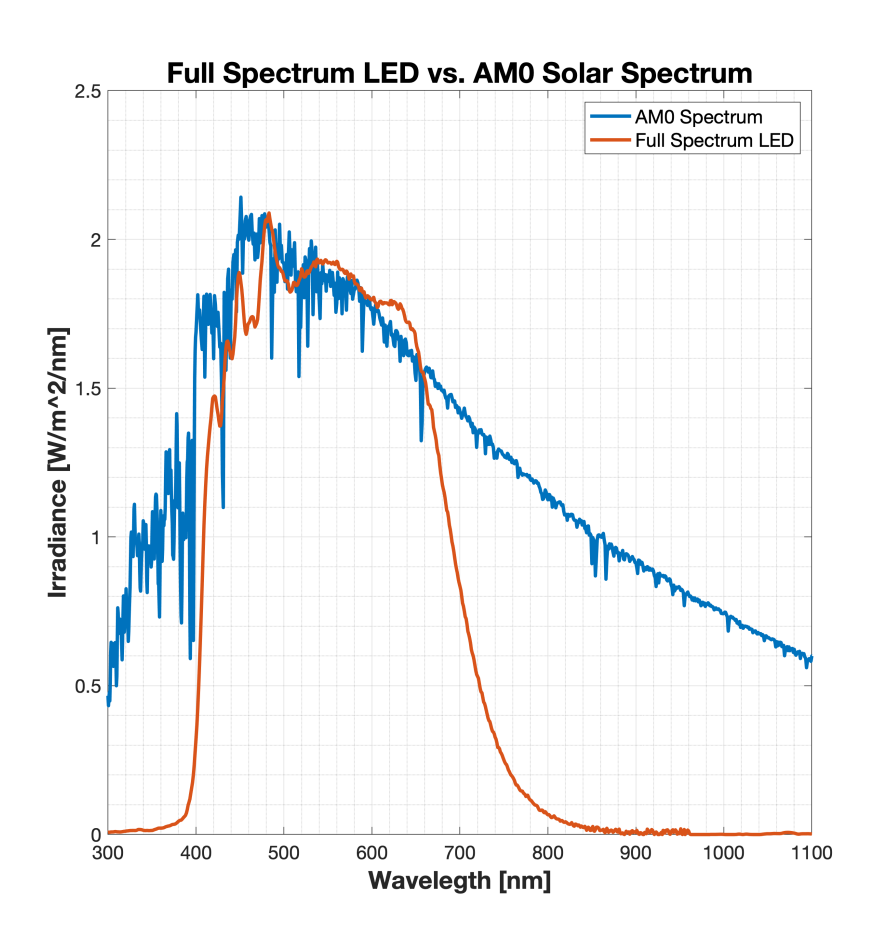
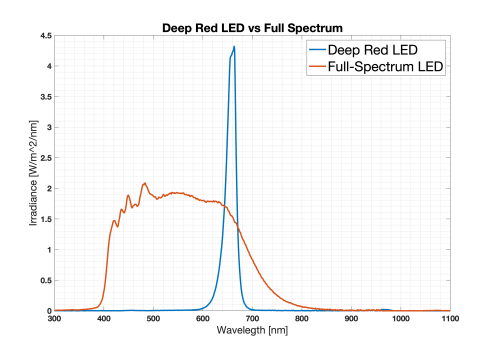
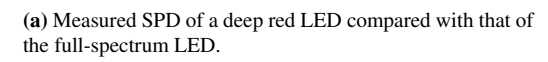
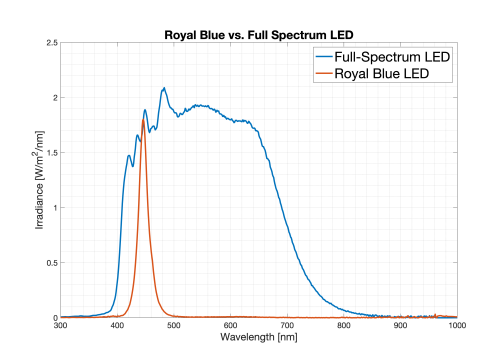


Figure 4.3: AM0 SPD ([49]) and the measured SPD of the full-spectrum LED.

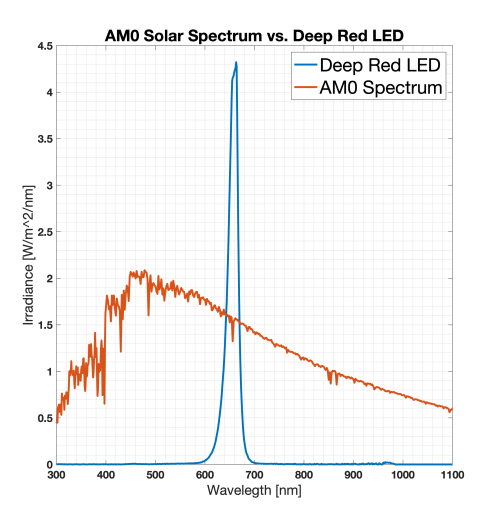




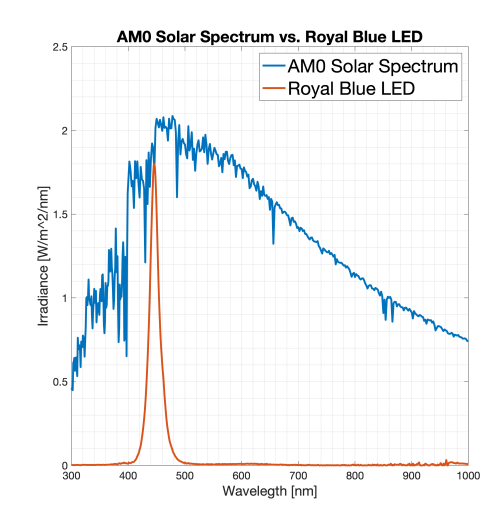


(b) Measured SPD of a royal blue LED above the corner of the receiver compared with the SPD of the full-spectrum LED directly above the center of the receiver.

Figure 4.4: Spectra of monochromatic deep red and royal blue LEDs, compared with that of a full-spectrum LED.



(a) Measured SPD of a deep red LED above the center of a receiver compared with the AM0 solar spectrum.



(b) Measured SPD of a royal blue LED above the corner of the receiver (right), compared with the AM0 spectrum.

Figure 4.5: AM0 solar spectrum compared with measured monochromatic LED spectra.

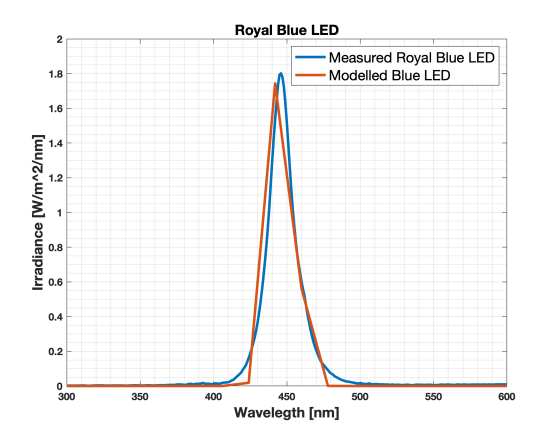


Figure 4.6: Measured SPD of a royal blue LED (see figure 4.5b) compared with the modelled SPD of a blue LED.

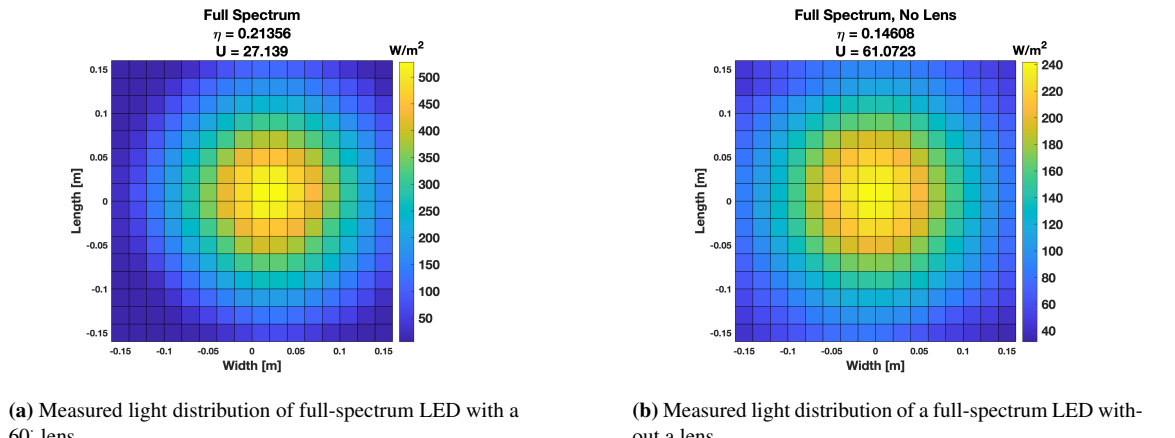


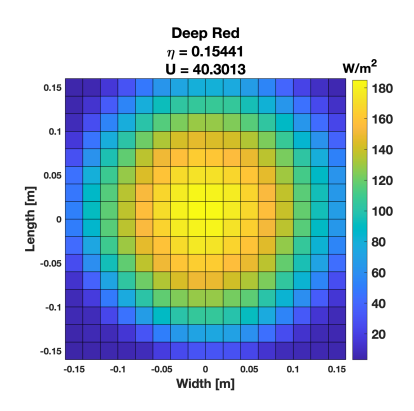
Figure 4.7: Measured light distributions of a full-spectrum LED.

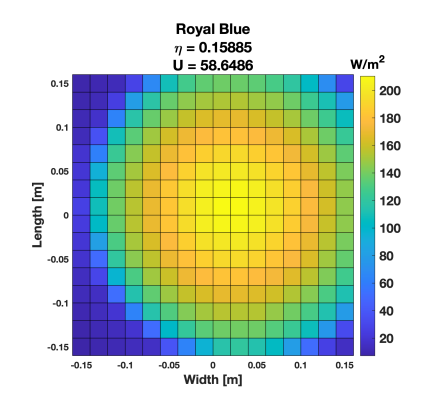
4.4 Distribution and Uniformity

For the light distribution of the LED, the spectrometer was used to measure the intensity of light at 289 points in a 32 cm by 32 cm grid. The light distribution and uniformity didn't specifically take into account the SPD, but only the intensity.

Figure 4.7 shows the measured light distribution of the full-spectrum LED with and without a 60° lens attached to the LED, at a distance of 0.21m from the receiver. It shows that while without a lens the efficiency is reduced from approximately 21% to 14.5%, the uniformity is greatly increased, from approximately 27.14 to 61.07. This is likely caused by the fact that without a lens the LED is closer to a Lambertian light source, with a wider angle-of-view (see section 2.6.1). For both of these measurements, an input power of 88.5W was used for the LED.

Figure 4.8 shows the light distributions from the two monochromatic LEDs, deep red and royal blue, with the 60° lens, from the same height of 0.21m as the previous measurements. The red LED was used with a 61.2W input power, due to its voltage limit of 24V, and the blue with 88.26W. These measurements show a lower efficiency compared to the full-spectrum measurements, yet a higher uniformity.





(a) Measured light distribution of a deep red LED with a 60 lens

(b) Measured light distribution of royal blue LED with a 60 lens

Figure 4.8: Measured light distributions of monochromatic LEDs.

4.5 Model Calibration

Because the models didn't take into account several unknown or imprecisely known parameters, the results of the experiments were used to calibrate the models to fit the different experimental results. This was done by running various models while incrementally adjusting the input parameters, and identifying the parameters that lead to the closest approximation to the experimental results. These were the input parameters:

- The x and y locations on the plane parallel to the receiver. This was initially adjusted from -0.02m to +0.02m in both directions in increments of 0.001m.
- The distance between the source and the receiver. This was adjusted in icrements of 0.001m from -0.02m to +0.02m relative to the measured height.
- The orientation of the light source towards the receiver, from -0.2rad to +0.2rad.
- The filter/concentration constant (see section 3.2.1. These were combined into one constant G and varied from 0.5 to 1.5.
- The mode number m (see section 2.6.1).

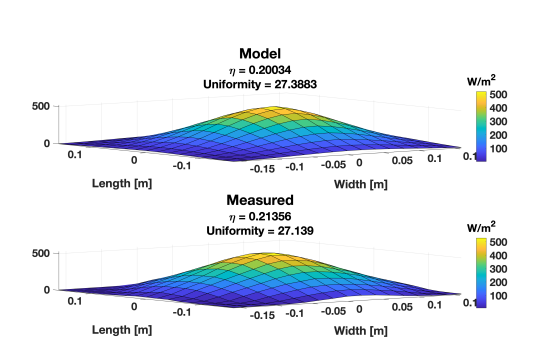
The RMSE between the models and the measurements was measured using the equation [50]:

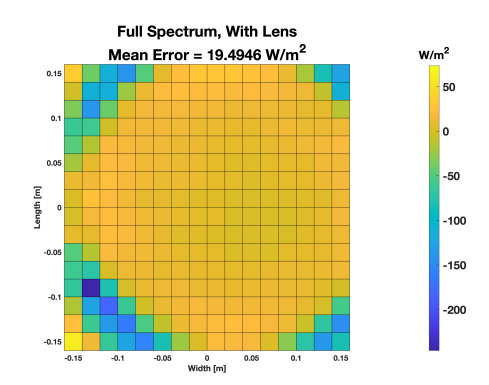
$$E = \sqrt{\frac{1}{n} \sum_{i=1}^{n} |A_i - M_i|^2},\tag{4.1}$$

where A is the actual measured intensity at each point and M is the intensity predicted by the modelled simulation. The model with the lowest RMSE relative to the experimental result was identified, and then another calibration was performed with a narrower range of parameter adjustments, specifically around the results of the initial calibration. In this second process, the models were calibrated based on three values: the lowest RMSE of the intensity; the lowest RMSE of the uniformity; and the lowest RMSE of the intensity combined with the lowest RMSE for the overall uniformity. In the combined RMSE, the uniformity was weighted by a factor of 10, i.e.:

LED	Measured η	Modelled η	Measured U	Modelled U	RMSE $[W/m^2]$
Full-spectrum	0.21356	0.20034	27.139	27.3883	19.4946
Full-spectrum, without lens	0.14608	0.14565	61.0723	59.6013	5.9044
Royal blue	0.15885	0.16316	58.6486	60.9771	22.1552
Deep red	0.15441	0.14967	40.3013	41.3139	12.1009

Table 4.1: Measured uniformities and efficiencies compared with those of the calibrated models.





(a) Comparison between measured and modelled light distribution of a full-spectrum LED.

(b) The error at each point of the grid between the measured and modelled light.

Figure 4.9: Model calibration for full Spectrum LED with a 60° lens.

$$E_{total} = E_{Intensity} + 10 \cdot E_{Uniformity},$$
 (4.2)

because otherwise the RMSE of the uniformity was seen to dominate the total RMSE.

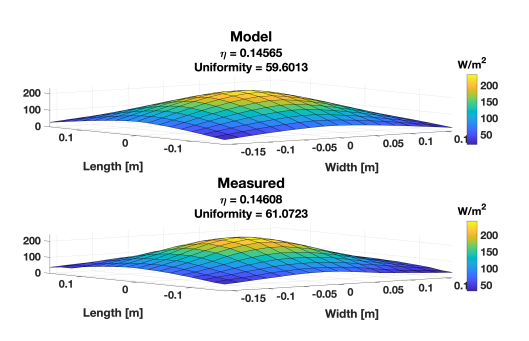
Table 4.1 presents the values found by using this combined RMSE, as it provided the closest values for both efficiency and uniformity on average.

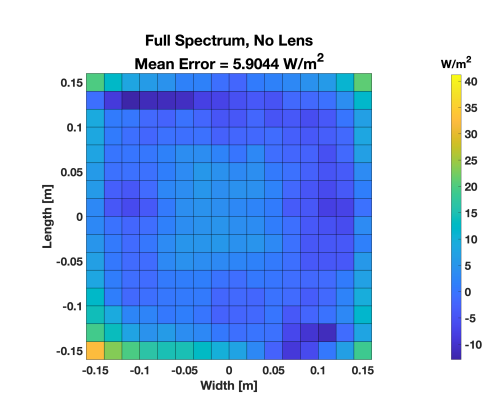
Figure 4.9a shows a comparison between the experimentally measured light distribution of the full-spectrum LED with a 60° lens, with the model calibrated for this measurement, and figure 4.9b shows the error between the intensities of the model and the measurement at each point on the grid. Figure 4.10 shows the results of the calibrated model for the same full spectrum LED without the lens attached. This model had the lowest mean error, under $6W/m^2$.

Figure 4.11 shows the results of the calibration with the royal blue LED. This is the model with the largest RMSE, at over $22W/m^2$, due to the large difference of values in the left edge and corners, as seen in figure 4.11b. The calibrated model for the deep red LED shown in 4.12 had a relatively low RMSE of approximately $12W/m^2$, and similarly its largest errors were in the left corners.

Some improvements in the calibrated models over the original models are due to the measured light source being slightly off-center or not precisely parallel to the receiver. The actual LEDs tend to have a higher factor of directivity f relative to the models. This suggests that they are not ideal Lambertian light sources, which would mean that the intensity is not proportional to the azimuth angle θ , or that their half-power angle $\theta_{1/2}$ is lower than the expected 60° (see section 2.6.1). Many of the biggest differences between measurement results and their corresponding calibrated models occurred at the edges and corners of the receiver.

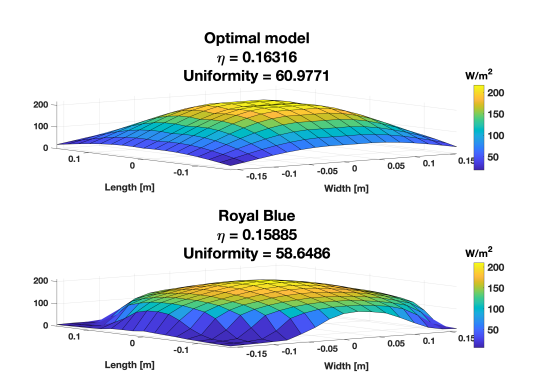
Overall, these simulations show that the models developed in chapter 3 can be used to model several types of light sources and the factors that affect their light distribution, with reasonably low error.

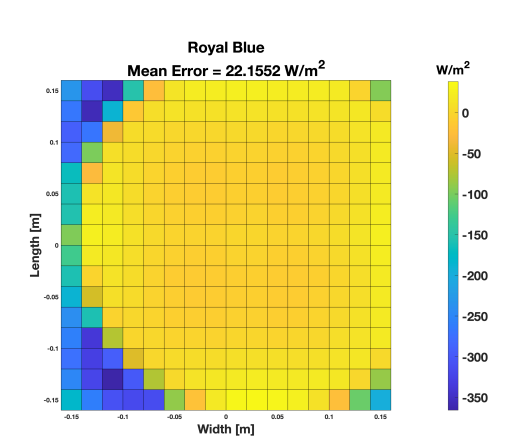




- (a) Comparison between measured and modelled light distribution of a full-spectrum LED without a lens.
 - **(b)** The error at each point of the grid between the measured and modelled light.

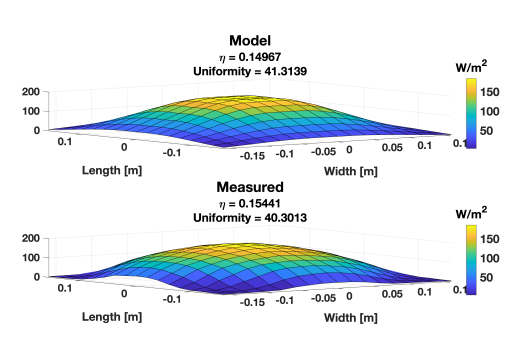
Figure 4.10: Calibration of the full-spectrum LED without a lens.

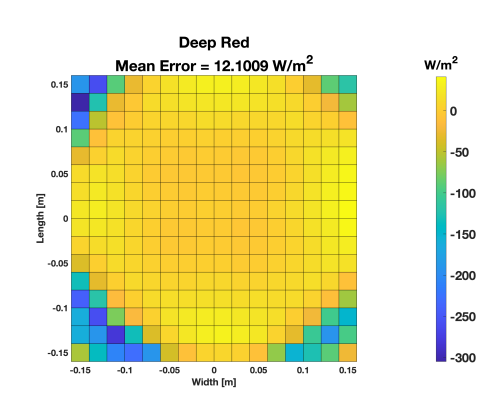




- (a) Comparison between measured and modelled light distribution of a Royal Blue LED with a lens.
 - (\mathbf{b}) The error at each point of the grid between the measured and modelled light of the royal blue LED.

Figure 4.11: Royal blue LED model calibration.





(a) Comparison between measured and modelled light distribution of a Deep Red LED with a lens.

(b) The error at each point of the grid between the measured and modelled light of the deep red LED.

Figure 4.12: Deep red LED model calibration.

4.6 Solar Simulator

In this section, in order to show a practical implementation of these light source models, a model for simulating the operation of outdoor VLC is described. This can be used to assist in designing actual solar simulators using a configuration of LEDs.

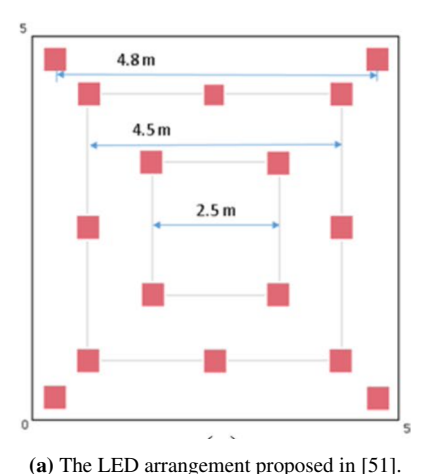
For outdoor conditions, an ambient sunlight of $1000 W/m^2$ is assumed. At first this was modelled by incorporating a very high input power combined with a very large distance between the source and receiver, thus simulating the sun's irradiation. An optical power of 2473705 W at a distance of 100m was found to yield a received power of approximately $1000W/m^2$ at a uniformity of close to 100%.

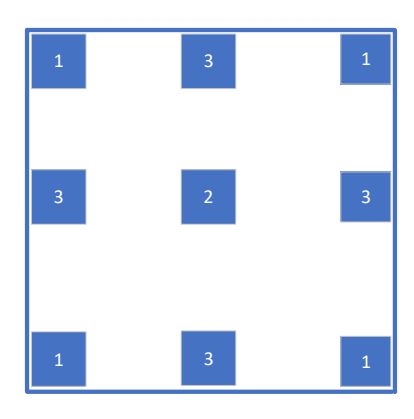
Next, in order to better accord with practical solar simulators, the model instead used a combination of 5 LEDs at a height of 0.4m. Four LEDs, with an optical power of 220W, were placed above the corners of the receiver, pointing slightly outward, away from the center, at an angle of 0.06rad or approximately 4° , so that there is less overlapping of the light from each source. One LED with an optical power of just 4W was placed above the center, to compensate for the lower intensity there due to its being at the largest distance from the corners. To increase the uniformity further, 4 additional LEDs, with an optical power of 31W, were added to the model above the center of each side of the receiver, where the intensity was lowest (see figure 4.13b). This brought the received optical power on the receiver to approximately $1000W/m^2$, at a uniformity of over 99.76. All LEDs were modelled as Lambertian sources with $\theta_{1/2} = 60^{\circ}$, i.e., m = 1.

More sophisticated configurations of light sources were considered, partly based on the models in [51] (see figure 4.13a), however the increases in uniformity this could bring about are very marginal, compared to the lower efficiencies and higher costs of such a configuration. Also, for this solar simulator, reflections were not taken into account, which could increase the uniformity while increasing the efficiency.

At this stage, only the light distribution was taken into consideration. The spectrum over the measurement area in this simulation corresponds to the spectrum of the full-spectrum LED, validated through SPD measurements in figure 4.3. The simulation can be further enhanced by considering light sources with different spectra, either by modelling them based on different parameters, or by fitting them to new measurements done with different light sources.

Superimposed on this ambient light is a time-varying signal, as shown in section 3.2.6. Depending on the range of the intensity of light (or alternatively, the distance of the light source, the concentration factor, etc.), the peak-to-peak intensity that can be used to transmit a signal varies, which leads to a variation in SNR, since the ambient light that acts as noise has less of an effect relative to the signal. To show the difference between different ranges of signal intensity, figure 4.15 shows the light distributions of 4





(b) 1) Four LEDs above the corners. 2) One additional LED above the center of the receiver. 3) Four additional LEDs above the middle of the edges.

Figure 4.13: Configurations of LEDs above a surface for improving uniformity.

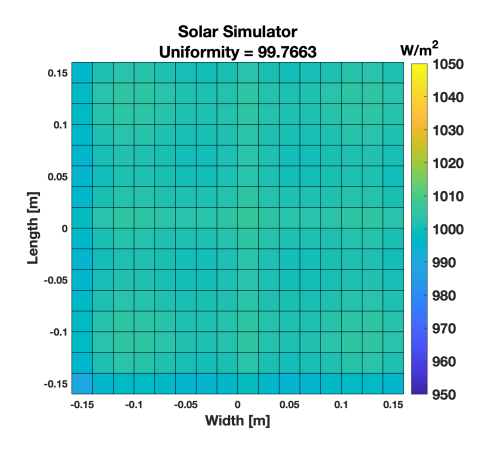


Figure 4.14: The Solar Simulator provides a uniform ambient light of $1000W/m^2$ on which modelled signals can be superimposed.

varying-intensity LEDs superimposed on the $1000 W/m^2$ uniform ambient light.

These simulations show one useful application of the framework developed in chapter 3. Figure 4.14 shows how the models were used to simulate outdoor ambient sunlight, with an intensity of approximately $1000W/m^2$ and a uniformity of over 99.7. Then, figure 4.15 shows how such a solar simulator can be used to model the peak-to-peak intensity of a time-varying VLC signal in outdoor ambient light conditions. As seen in section 2.3 with a larger the peak-to-peak intensity, a better data-rate can be achieved [13].

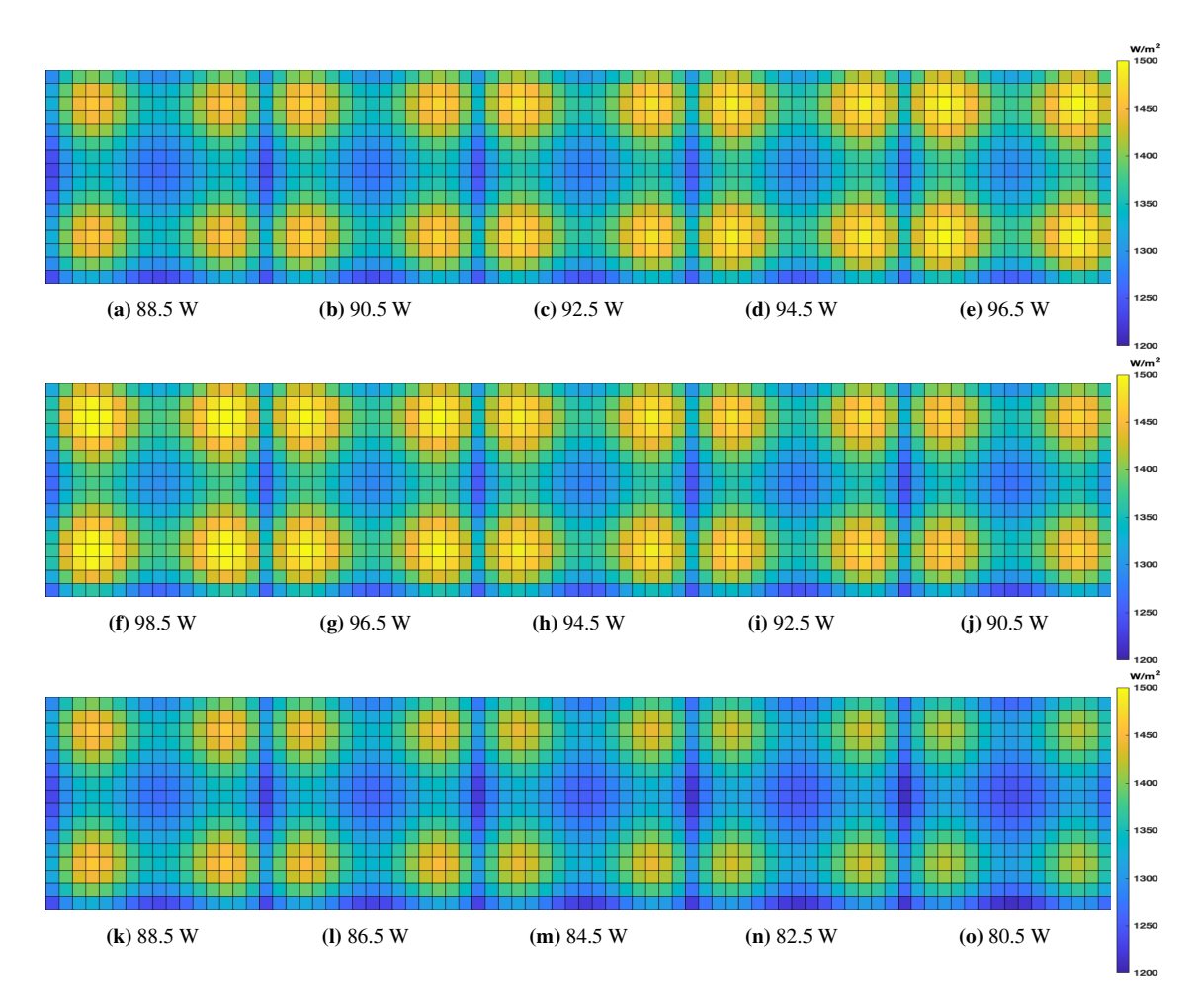


Figure 4.15: Light with a step-function of varying optical power from 80.5 W to 98.5 W, superimposed on the solar simulator's uniform ambient light of $1000W/m^2$

Chapter 5

Conclusion and Recommendations

This thesis presents a system for characterising VLC light sources by modeling their SPDs and the distribution of the light they emit onto a receiver. This includes a variety of modes of operation, such as multiple light sources, multiple light paths from source to receiver, and time-variation, that can affect the efficiency and optimality of a VLC system. This is meant to enable the prediction of the behaviour of VLC systems, as well as aid in designing such systems to match desired behaviours.

The modelled distributions and uniformities were validated through experimental measurements, however at first the measured efficiencies were somewhat lower than predicted by the models. These measurements were then used to calibrate the models accordingly, which often involved increasing the factor f, which is a measure of the directivity of the light source, whereby the intensity of received light drops exponentially with an increase in the angle of incidence, i.e. farther from the center of the viewing angle. This is probably due to the fact that the LEDs were not ideal Lambertian light sources, particularly when a focusing lens was attached to them. With bare LEDs, without a lens, the light distribution was found to be more uniform, however this comes at the expense of lower efficiency.

The models show that the uniformity that can be achieved with four LEDs is much better than a single LED placed above the center of a receiver, however this comes with a decrease in efficiency. Conversely, reflective surfaces can be used advantageously to increase the efficiency of light from source to receiver, while diminishing the uniformity of the light distribution. The larger the surface area, the higher the efficiency that the system can achieve, however this likewise decreases the uniformity.

When it comes to outdoor VLC, the signal must overcome the noise due to ambient sunlight. This means that the peak-to-peak intensity of the modulated light signal should be as high as possible, and the solar simulator modelled in section 4.6 provide a metric for determining the viability of such a signal. Likewise, the frequency of the signal is limited due to the capacitance of a PV receiver and its frequency-response. These two factors place a limit on the maximum achievable data-rate of a PV-based VLC link, and should be further explored in future studies.

The models presented in chapter 3 were calibrated based on a limited set of experiments, within a narrow range of parameters. The accuracy of the models can be improved by conducting more experimental analyses with a wider variety of LEDs and configurations. In the future, LASERs, which have a much more focused directivity, can be taken into account, as well as underwater environments, which could yield very different output parameters.

Future models should also consider the intensity of light in specific intervals of wavelengths. Using a monochromatic light source, combined with a bandpass filter at the receiver, could allow for VLC systems with much better performance under outdoor ambient light, as seen in the comparison between the SPDs of the full-spectrum LED and monochromatic LEDs in chapter 4. Spectrum dependence would affect the multipath models, where ρ can be wavelength dependent.

Acknowledgements

This master's thesis was conducted at the Photovoltaic Materials and Devices (PVMD) group, at the faculty of Electrical Engineering, Mathematics and Computer Science (EEMCS) in Delft University of Technology. It was supervised by Prof. Olinda Isabella, Dr. Patrizio Manganiello and Dr. Mirco Muttillo.

I want to thank my supervisors. Over the course of many meetings, they have helped me a lot with this thesis project, and taught me many useful things. Beyond that, they have greatly inspired me.

I also want to thank my family and friends, who supported and encouraged me throughout my work on this project.

Appendix A

Software

A.1 Light Distribution

```
1 %Generating a model of the light distribution over a receiver surface
2 %Input power [W]:
3 OpticalPower = 100;
4 %Location relative to the center of the receiver [m]:
_{5} xlocation = 0;
_{6} ylocation = 0;
_{7} height = 0.25;
8 %Direction relative to a 90 deg angle of incidence [rad]:
9 \text{ angle } 1 = 0;
angle2 = 0;
" %Ambient light [W]:
12 ambient = 0;
13 %Reflectance coefficient:
_{14} rho = 1;
15 %Filtering/Concentration factor:
_{16} G = 1;
17 %Directivity factor:
_{18} m = 1;
  %Received Light Intensity:
  Distribution = dis(OpticalPower, xlocation, ylocation, height, angle1,
      angle2, ambient, rho, G, m);
23 %Uniformity:
  Uniformity=uni(Distribution);
26 %Efficiency:
27 Ppercell = (Distribution).* Arcell;
TRP2 = sum(Ppercell, 'all');
29 TRP=round(TRP2,2);
officiency=TRP/OpticalPower;
```

```
32 %x and y axes:
xax = -0.16:0.02:0.16;
  yax = -0.16:0.02:0.16;
  %Graph
  figure
  surf(xax, yax, Distribution);
  cb2=colorbar
h = gca;
 h. YAxis. FontWeight = 'bold';
  h. XAxis. FontWeight = 'bold';
  view([0 90])
  title ('Model', 'fontweight', 'bold', 'fontsize', 16)
  txtRP = ['\eta = ' num2str(efficiency), newline 'U = ' num2str(
      Uniformity)];
  subtitle (txtRP, 'fontweight', 'bold', 'fontsize', 16)
  xlabel('Width [m]', 'fontweight', 'bold', 'fontsize', 14)
  ylabel ('Length [m]', 'fontweight', 'bold', 'fontsize', 14)
  title (cb2, 'W/m^2', 'fontweight', 'bold', 'fontsize', 14)
  h.FontWeight = 'bold';
  function Proptxy=dis(Popt, xlocation, ylocation, height, angle1, angle2,
52
       ambient, rho, G, m)
53 %Input power:
  Ptopt = Popt;
  %Angle of View:
  theta = 2*pi/3; %120 deg
  halftheta = theta/2; \%60 deg
  %G = Gconc * Gfilter
  %m - mode number
  count = 1;
  count2 = 1;
62
  for l = (x location - 0.16) : 0.02 : (x location + 0.16)
63
       phix = [tan(abs(1)/height)];
       for w=(ylocation -0.16):0.02:(ylocation +0.16)
               phiy = [tan(abs(w)/height)];
66
               p1 = (\cos(phix + angle1));
67
               p2 = (\cos(phiy + angle2));
               if (phix < halftheta) && (phiy < halftheta)
                   Proptxy (count, count2)=rho*G*(0.5*(m+1))*((Ptopt*G1*(p1^m))
70
                       ).*(p2^m)/(pi*(sqrt((height^2)+(1^2)+(w^2))^2));
               e1se
71
                   Proptxy (count, count2) = 0;
72
73
               count2 = count2 + 1;
74
       end
75
       count = count + 1;
       count2 = 1;
```

```
78 end79 end
```

A.2 Light Uniformity

```
function Uniformity=uni(Distribution)

M=mean(Distribution, 'all');
[MinLight, MaxLight]=bounds(Distribution, 'all');

Uniformity1=0;
for i=1:1:17
for j=1:1:17
Uniformity1 = Uniformity1 + (abs(Distribution(i,j)-M))/M;
end

uniformity2 = abs(Uniformity1/(17*17));
Uniformity= (1-Uniformity2)*100;
end
```

Bibliography

- [1] M. Nakagawa, "Visible light communications," 2007.
- [2] P. Hoeher, Visible Light Communications: Solutions Manual. Carl Hanser Verlag GmbH & Company KG, 2019, ISBN: 9783446463035. [Online]. Available: https://books.google.nl/books?id=i16yDwAAQBAJ.
- [3] A. Beling and J. C. Campbell, "High-speed photodiodes," *IEEE Journal of Selected Topics in Quantum Electronics*, vol. 20, pp. 57–63, 2014.
- [4] N. Rathee, S. Nagpal, A. Malik, and C. Khandelwal, "An efficient intelligent system for data communication using life technology 1," *International Journal of Computers and Technology*, vol. 13, pp. 5044–5050, Aug. 2014. DOI: 10.24297/ijct.v13i10.2326.
- [5] S. Louvros and D. Fuschelberger, "Vlc technology for indoor lte planning," pp. 21–41, Aug. 2013. DOI: 10.1007/978-3-319-00663-5-2.
- [6] H. Haas, L. Yin, Y. Wang, and C. Chen, "What is lifi?" *Journal of Lightwave Technology*, vol. 34, no. 6, pp. 1533–1544, 2016. DOI: 10.1109/JLT.2015.2510021.
- [7] M. F. Ali, D. N. K. Jayakody, and Y. Li, "Recent trends in underwater visible light communication (uvlc) systems," *IEEE Access*, vol. 10, pp. 22169–22225, 2022. DOI: 10.1109/ACCESS.2022. 3150093.
- [8] D. N. Amanor, W. W. Edmonson, and F. Afghah, "Intersatellite communication system based on visible light," *IEEE Transactions on Aerospace and Electronic Systems*, vol. 54, pp. 2888–2899, 2018.
- [9] A. K. Majumdar, "Laser-based satellite and inter-satellite communication systems: Advanced technologies and performance analysis," in *Laser Communication with Constellation Satellites, UAVs, HAPs and Balloons: Fundamentals and Systems Analysis for Global Connectivity.* Cham: Springer International Publishing, 2022, pp. 199–229.
- [10] M. I. Gabr, "Data transmission via visible light communication (vlc) technique," *International Journal of Innovative Research in Science, Engineering and Technology*, vol. 5, pp. 16473–16481, Sep. 2016. DOI: 10.15680/IJIRSET.2016.0509133.
- [11] M. Kowalczyk and J. Siuzdak, "Influence of reverse bias on the leds properties used as photo-detectors in vlc systems," Sep. 2015, p. 966 205. DOI: 10.1117/12.2197831.
- [12] H. Ziar, P. Manganiello, O. Isabella, and M. Zeman, "Photovoltatronics: Intelligent pv-based devices for energy and information applications," *Energy Environ. Sci.*, vol. 14, pp. 106–126, 1 2021. DOI: 10.1039/D0EE02491K. [Online]. Available: http://dx.doi.org/10.1039/D0EE02491K.
- [13] S. Das, A. Sparks, E. Poves, S. Videv, J. Fakidis, and H. Haas, "Effect of sunlight on photovoltaics as optical wireless communication receivers," *Journal of Lightwave Technology*, vol. PP, pp. 1–1, Jul. 2021. DOI: 10.1109/JLT.2021.3096734.

- [14] D. A. van Nijen, P. Manganiello, M. Zeman, and O. Isabella, "Exploring the benefits, challenges, and feasibility of integrating power electronics into c-si solar cells," *Cell Reports Physical Science*, vol. 3, no. 7, p. 100944, 2022, ISSN: 2666-3864. DOI: https://doi.org/10.1016/j.xcrp. 2022.100944. [Online]. Available: https://www.sciencedirect.com/science/article/pii/S2666386422002259.
- [15] A. Flikweert, "Visible light communication with solar panels," 2022.
- [16] P. A. Haigh, Visible Light, ser. 2053-2563. IOP Publishing, 2020, ISBN: 978-0-7503-1680-4.
- [17] N. Chi, *LED-Based Visible Light Communications*, ser. Signals and Communication Technology. Springer Berlin Heidelberg, 2018, ISBN: 9783662566602. [Online]. Available: https://books.google.nl/books?id=YaNsDwAAQBAJ.
- [18] S. A. Fortuna. "Ee 232: Lightwave devices, lecture #22 photodetector noise." (), [Online]. Available: https://inst.eecs.berkeley.edu/~ee232/sp19/lectures/Lecture%20-%20Photodetector% 20Noise.pdf.
- [19] Z. Ghassemlooy, W. O. Popoola, and S. Rajbhandari, "Optical wireless communications: System and channel modelling with matlab®," 2012.
- [20] A. Bali. "Signal to noise ratio formula: Calculation, statistics & examples." (), [Online]. Available: https://collegedunia.com/exams/signal-to-noise-ratio-formula-calculation-statistics-examples-science-articleid-4583.
- [21] M. S. Ab-Rahman, N. I. Shuhaimi, L. A. H. Azizan, and M. R. Hassan, "Analytical study of signal-to-noise ratio for visible light communication by using single source," *Journal of Computer Science*, vol. 8, pp. 141–144, 2012.
- [22] S. Yijie and W. Yongsheng, "A half bit interleaved rz-ook modulation for led based visible light communication," Nov. 2018, pp. 119–121, ISBN: 978-1-4503-6585-7. DOI: 10.1145/3291842. 3291924.
- [23] Z. Wang, W.-D. Zhong, C. Yu, and J. Chen, "A novel led arrangement to reduce snr fluctuation for multi-user in visible light communication systems," in 2011 8th International Conference on Information, Communications & Signal Processing, 2011, pp. 1–4. DOI: 10.1109/ICICS.2011.
- [24] J. Fakidis, H. Helmers, and H. Haas, "Simultaneous Wireless Data and Power Transfer for a 1-Gb/s GaAs VCSEL and Photovoltaic Link," *IEEE Photonics Technology Letters*, vol. 32, pp. 1277–1280, 2020.
- [25] W. Shockley and H. J. Queisser, "Detailed balance limit of efficiency of p-n junction solar cells," *Journal of Applied Physics*, vol. 32, pp. 510–519, 1961.
- [26] N. Shinohara, "Power without wires," IEEE Microwave Magazine, vol. 12, S64–S73, 2011.
- [27] J. Xue, Z. Li, and R. J. Ram, "Irreversible thermodynamic bound for the efficiency of light-emitting diodes," *Phys. Rev. Appl.*, vol. 8, p. 014017, 1 Jul. 2017. DOI: 10.1103/PhysRevApplied.8.014017. [Online]. Available: https://link.aps.org/doi/10.1103/PhysRevApplied.8.014017.
- [28] D. Neamen, Semiconductor Physics And Devices. McGraw-Hill Education, 2011, ISBN: 9780073529585.
- [29] "Pn junction diode." (), [Online]. Available: https://www.electronics-tutorials.ws/diode/diode_3.html.
- [30] "MIT OpenCourseWare, Lecture 19-20, Light Emitting Diodes." (2013), [Online]. Available: %5Curl% 7Bhttps://ocw.mit.edu/courses/3-024-electronic-optical-and-magnetic-properties-of-materials-spring-2013/0bala47f71a8843b0e45b9aa2e66a875_MIT3_024S13_2012lec19-20.pdf%7D.

- [31] J. Cho, J. H. Park, J. K. Kim, and E. F. Schubert, "White light-emitting diodes: History, progress, and future," *Laser & Photonics Reviews*, vol. 11, no. 2, p. 1600147, 2017. DOI: https://doi.org/10.1002/lpor.201600147. [Online]. Available: https://onlinelibrary.wiley.com/doi/abs/10.1002/lpor.201600147.
- [32] H. Lu, Q. Song, X. Xu, et al., "Improving the CRI of Al2O3-YAG:Ce eutectic for high-power white LEDs applications: Energy-transfer and co-luminescence," Optical Materials, vol. 121, p. 111415, 2021, ISSN: 0925-3467. DOI: https://doi.org/10.1016/j.optmat.2021.111415. [Online]. Available: %5Curl % 7Bhttps://www.sciencedirect.com/science/article/pii/S0925346721006169%7D.
- [33] S. Thomson, "Time-resolved electroluminescence spectroscopy of a white light emitting diode," Jul. 2018
- [34] L. Cui, Y. Tang, H. Jia, J. Luo, and B. Gnade, "Analysis of the multichannel wdm-vlc communication system," *Journal of Lightwave Technology*, vol. 34, no. 24, pp. 5627–5634, 2016. DOI: 10.1109/JLT.2016.2623759.
- [35] S. P. Ying, C.-W. Tang, and B.-J. Huang, "Charaterizing leds for mixture of colored led light sources," in 2006 International Conference on Electronic Materials and Packaging, 2006, pp. 1–5. DOI: 10. 1109/EMAP.2006.4430677.
- [36] Y. Huang, E.-L. Hsiang, M.-Y. Deng, and S.-T. Wu, "Mini-LED, Micro-LED and OLED displays: present status and future perspectives," *Light: Science & Applications*, vol. 9, Dec. 2020. DOI: 10. 1038/s41377-020-0341-9.
- [37] Z. Nazari Chaleshtori, S. Zvanovec, Z. Ghassemlooy, H. Eldeeb, and M. Uysal, "A flexible oled vlc system for an office environment," Jul. 2020. DOI: 10.1109/CSNDSP49049.2020.9249613.
- [38] S. Han, C. Xu, H. Li, *et al.*, "AlGaInP-based Micro-LED array with enhanced optoelectrical properties," *Optical Materials*, vol. 114, 2021, ISSN: 0925-3467. DOI: https://doi.org/10.1016/j.optmat.2021.110860. [Online]. Available: %5Curl%7Bhttps://www.sciencedirect.com/science/article/pii/S0925346721000616%7D.
- [39] S. Zhu, P. Qiu, X. Shan, *et al.*, "High-speed long-distance visible light communication based on multicolor series connection micro-leds and wavelength division multiplexing," *Photon. Res.*, vol. 10, no. 8, pp. 1892–1899, Aug. 2022. DOI: 10.1364/PRJ.459531. [Online]. Available: https://opg.optica.org/prj/abstract.cfm?URI=prj-10-8-1892.
- [40] T. Komine, J. Lee, S. Haruyama, and M. Nakagawa, "Adaptive equalization system for visible light wireless communication utilizing multiple white led lighting equipment," *IEEE Transactions on Wireless Communications*, vol. 8, 2009.
- [41] A. H. Kitai, "Principles of solar cells, leds and diodes: The role of the pn junction," 2011.
- [42] I. Ashdown and K. Man, "Accurate colorimetric feedback for rgb led clusters," vol. 6337, Aug. 2006. DOI: 10.1117/12.683239.
- [43] A. Thorseth, J. Thomsen, and C. Dam-Hansen, "Characterization, modeling, and optimization of light-emitting diode systems," Ph.D. dissertation, Jan. 2011, p. 69.
- [44] W.-C. Chen, T.-T. Lai, M.-W. Wang, and H.-W. Hung, "An optimization system for led lens design," *Expert Systems with Applications*, vol. 38, no. 9, pp. 11976–11983, 2011, ISSN: 0957-4174. DOI: https://doi.org/10.1016/j.eswa.2011.03.092. [Online]. Available: https://www.sciencedirect.com/science/article/pii/S0957417411005136.
- [45] L. Svilainis and V. Dumbrava, "Numerical comparison of led directivity approximation functions for video displays," *Displays*, vol. 31, pp. 196–204, Dec. 2010. DOI: 10.1016/j.displa.2010.08.001.

- [46] H.-G. Hao, D.-D. Zhang, and S. Tang, "Analysis of the led lamp arrangement for uniformity of illumination in indoor vlc system," *Journal of the Optical Society of Korea*, vol. 18, Dec. 2014. DOI: 10.3807/JOSK.2014.18.6.663.
- [47] "Lcfocus." (), [Online]. Available: https://www.aliexpress.com/store/2335145?spm=a2g0o.detail.1000023.5.5fb93153rQWwet.
- [48] Spectral Evolution SR-1901PT Portable Spectroradiometer for Pulsed Solar Simulators, Spectral Revolution, 2018. [Online]. Available: %5Curl %7Bhttps://s3-us-east-2.amazonaws.com/spectralevolution/assets/SR-1901PT_Flyer_62619.pdf%7D.
- [49] "National renewable energy laboratory." (), [Online]. Available: https://www.nrel.gov/grid/solar-resource/smarts-files.html.
- [50] "Root-mean-square error between arrays." (2022), [Online]. Available: %5Curl%7Bhttps://www.mathworks.com/help/matlab/ref/rmse.html#mw_98b141b0-ce2c-4211-8f39-ba00b7586eb7_vh%7D.
- [51] N. Mahfouz, H. Fayed, A. Aziz, and M. Aly, "Improved light uniformity and SNR employing new LED distribution pattern for indoor applications in VLC system," *Optical and Quantum Electronics*, vol. 50, Sep. 2018. DOI: 10.1007/s11082-018-1618-6.